Title

From nutrients to fish: Impacts of mesoscale processes in a global CESM-FEISTY eddying ocean model framework

Authors

Krumhardt, Kristen M

Long, Matthew C

Petrik, Colleen M

et al.

Publication Date

2024-09-01

DOI

10.1016/j.pocean.2024.103314

From nutrients to fish: Impacts of mesoscale processes in a global CESM-FEISTY eddying ocean model framework

Kristen M. Krumhardt[1*], Matthew C. Long[1,2], Colleen M. Petrik[3], Michael Levy[1], Frederic S. Castruccio[1], Keith Lindsay[1], Lev Romashkov[1], Anna-Lena Deppenmeier[1], Rémy Denéchère[3], Zhuomin Chen[4], Laura Landrum[1], Gokhan Danabasoglu[1], Ping Chang[5]

May 21, 2024

[1]Climate and Global Dynamics, NSF National Center for Atmospheric Research, Boulder, Colorado, U.S.A.
[2][C]Worthy, Boulder, Colorado, U.S.A.
[3]Scripps Institution of Oceanography, University of California San Diego, La Jolla, California, U.S.A.
[4]Department of Marine Sciences, University of Connecticut, Groton, Connecticut, U.S.A.
[5]Department of Oceanography, Texas A&M University, College Station, Texas, U.S.A.

*Corresponding author: kristenk@ucar.edu

Keywords: marine ecosystems, mesoscale processes, fish modeling, Earth System Model, high resolution

Abstract

The ocean sustains ecosystems that are essential for human livelihood and habitability of the planet. The ocean holds an enormous amount of carbon, and serves as a critical source of nutrition for human societies worldwide. Climate variability and change impacts marine biogeochemistry and ecosystems. Thus, having state-of-the-art simulations of the ocean, which include marine biogeochemistry and ecosystems, is critical for understanding the role of climate variability and change on the ocean biosphere. Here we present a novel global eddy-resolving (0.1° horizontal resolution) simulation of the ocean and sea ice, including ocean biogeochemistry, performed with the Community Earth System Model (CESM). The simulation is forced by the atmospheric dataset based on the Japanese Reanalysis (JRA-55) product over the 1958 – 2021 period. We present a novel configuration of the CESM marine ecosystem model in this simulation which includes two zooplankton classes: microzooplankton and mesozooplankton. This novel planktonic food web structure facilitates "offline" coupling with the Fisheries Size and Functional Type (FEISTY) model. FEISTY is a size- and trait-based model of fish functional types contributing to fisheries. We present an evaluation of the ocean biogeochemistry, marine ecosystem (including fish types), and sea ice in this high-resolution simulation compared to available observations and a corresponding low resolution (nominal 1°) simulation. Our analysis offers insights into environmental controls on trophodynamics within the ocean. We find that this high resolution simulation provides a realistic reconstruction of nutrients, oxygen, sea ice, plankton and fish distributions over the global ocean. On global and large regional scales the high-resolution simulation is comparable to the standard 1° simulation, but on smaller scales, explicitly resolving the mesoscale dynamics is shown to be important for accurately capturing trophodynamic structuring, especially in coastal ecosystems. We show that fine scale ocean features leave imprints on ocean ecosystems, from plankton to fish, from the tropics to polar regions. This simulation also offers insights on ocean acidification over the past 64 years, as well as how large scale climate variations may impact upper trophic levels. The data generated by the simulations are publicly available and will be a fruitful community resource for a large variety of oceanographic science questions.

1 Introduction

The ocean plays a prominent role in our Earth system, holds tremendous biodiversity, and provides nutrition and culture to human societies. The ocean is the dominant active reservoir of carbon –

storing roughly 38,000 Pg C of natural carbon – and it is a major sink for atmospheric CO_2, absorbing approximately one-quarter of human-generated CO_2 emissions annually (Friedlingstein et al., 2022). Ocean ecosystems are critical to food security: fish, crustaceans, and molluscs are an essential source of nutrition for much of the world's population, with fish accounting for roughly 17% of animal protein consumed (FAO, 2018). Fisheries are both culturally important and economically vital—contributing, for instance, over $200 billion in U.S. economic activity and more than 1.7 million jobs in the U.S. annually (NMFS, 2018). The ocean also contains 90% of the habitable space on Earth and is home to species from all clades of life too numerous to count (COML, 2010). Preserving this biodiversity in the face of human impact is essential for the continued habitability of our planet (Worm et al., 2006).

An ability to understand, predict, and proactively manage human use and impacts on marine ecosystems is a critical societal need – one that is particularly urgent in the context of climate change and the increasing footprint of human activities. The ocean has absorbed ∼90% of the anomalous heat trapped due to rising atmospheric CO_2 concentrations (Cheng et al., 2017) and ocean circulation strongly determines regional climate (e.g., see Palter, 2015, for an how the Gulf Stream influences European climate). Warming, acidification, and loss of dissolved oxygen from the ocean constitute ecosystem stressors (e.g., Gruber, 2011) that are unprecedented in the history of life and pose significant risk of large-scale extinctions (Penn & Deutsch, 2022).

Comprehensive models of the ocean ecosystem are an essential element for understanding the impacts of global change on the ocean biosphere. Earth system models (ESMs), while originally developed for the purpose of simulating carbon-climate feedbacks (Friedlingstein et al., 2006), have relevance to questions related to ocean ecosystems (Bopp et al., 2013; Stock et al., 2011; Tommasi et al., 2017). Notably, ESMs represent mechanistic linkages between the physical climate system and marine ecosystems. Three-dimensional ocean general circulation models are coupled with ocean biogeochemical models (OBMs) that represent the lower trophic levels of marine ecosystems (i.e., plankton) that play a key role in mediating carbon fluxes and elemental cycles of nutrients, such as nitrogen and phosphorus. Primary productivity converts inorganic nutrients and carbon in the sunlit surface ocean to organic matter; the sinking and remineralization of this material constitute "the biological pump": a mechanism sequestering carbon at depth, as well as providing benthic organisms with a food resource, especially in coastal shelf regions. Net primary productivity (NPP) by phytoplankton supports nearly all marine life and is tightly controlled by physical processes which control nutrient and light availability. Marine phytoplankton account for roughly half of the globally-integrated annual NPP, but with only ∼1% of the photosynthetic biomass of that on land (Field et al., 1998). Lacking biomass-derived inertia typical of terrestrial systems, planktonic marine ecosystems are sensitive to perturbation by short-timescale variations in physical forcing (e.g., see Rousseaux & Gregg, 2012).

As the ultimate supply of energy to higher trophic levels, NPP places an upper limit on ecosystem production; however, relationships between, for instance, fisheries yields and NPP are not straightforward (Stock et al., 2017; Straile, 1997). In particular, a variety of ecological mechanisms modulate trophodynamics contributing to variable higher trophic levels yields. OBMs are capable of simulating the large-scale distribution of NPP associated biogeography (e.g., Follows et al., 2007), and the dynamic response of lower-trophic levels to climate variability and change (Stock et al., 2014a; Stock et al., 2014b). Simulated ocean biogeochemical dynamics are driven by bottom-up forcing: physical processes regulate temperature distributions and nutrient supply to the euphotic zone, mixed layer depths control light availability and biomass concentrations; these processes together affect phytoplankton growth directly by modulating resource availability and influence which types of phytoplankton thrive (Doney et al., 2006). Simultaneously, zooplankton respond in the context of environmentally-dependent rate processes, changes in prey concentrations, and community composition. State-of-the-art OBMs represent zooplankton grazing explicitly, which is a fundamental control on phytoplankton bloom dynamics (e.g., Behrenfeld & Boss, 2014; Friedland et al., 2016) and export of organic matter from the surface ocean (Turner, 2015). However, OBMs, including the one we present in this study, do not typically have an explicit representation of higher-trophic-level predation on zooplankton, relying instead on a nonlinear density-dependent loss term that implicitly represents predation (i.e., "closure" term; e.g., Edwards & Yool, 2000; Fasham, 1995; Ohman & Hirche, 2001; Steele & Henderson, 1992).

Physical regimes structure the upper-ocean habitat, but ecosystem processes further modulate trophic energy transfers and the trophic efficiency of marine ecosystems is regionally variable (Ryther, 1969). In the oligotrophic systems characteristic of subtropical gyres, for instance, nutrient supply is limited by strong stratification; algal assemblages are dominated by small-celled organisms with high

nutrient-uptake efficiencies. Planktonic food webs in these systems are tightly coupled, dominated by microzooplankton grazers, high rates of upper-ocean recycling, and little material available for export or consumption by higher trophic levels. High latitude systems, by contrast, tend to be nutrient replete, but light-limited and strongly seasonal; these systems are dominated by larger phytoplankton and tend to export greater fractions of primary production - either as sinking organic matter or up the food chain. Further, continental shelves tend to have a large benthic component, fueled by particulate organic carbon (POC) falling to the seafloor, where it is consumed by benthic organisms. While OBMs simulate zooplankton and POC dynamics, additional model efforts need to be made to understand, e.g., the impacts of climate change and variability on fisheries.

Predicting fish biomass and productivity globally is one of the current challenges in fisheries ecology. This is typically done by using size- and/or trait-based representations of fish (K. Andersen, 2019; Kiørboe et al., 2018). Projections of fish biomass and productivity are made by forcing fish models with ESM output, allowing an assessment of the implications of climate change on higher trophic levels in marine environments (Heneghan et al., 2021; Lotze et al., 2019; Maury, 2010; Petrik et al., 2020). The Fisheries and Marine Ecosystem Model Intercomparison Project (FishMIP), for example, projected a 5% change in marine animal biomass for every 1° of warming. In these models, fish are subject to bottom-up drivers, i.e., prey biomass, temperature, or mixed layer depth. Previous work has acknowledged the effect of climate change on fish biomass: for example, Lotze et al. (2019) showed that declines in NPP are amplified in ocean animal biomass (i.e., trophic amplification). Further, ESM-forced fish models have shown that large pelagic fishes may be most sensitive to climate change (Heneghan et al., 2021; Petrik et al., 2020). Most of these simulations, including the one documented in this study, are run in an "offline" configuration, meaning that coupling between the OBM and the fish model is one directional; i.e., the fish model uses outputs from the OBM. "Online" simulations have two-way coupling, meaning that fish predation could feedback on the zooplankton, as well as representing a more complete cycling of carbon and nutrients. Indeed, Dupont et al. (2023) have documented the impacts of feedbacks between the OBM and high trophic levels (HTL), showing that implementing two-way coupling generates shifts in NPP, plankton dynamics, and HTL.

Notably, however, most ESMs are typically integrated at a horizontal resolution of about 1° or 100 km. This coarse grid-spacing precludes resolving the ocean mesoscale (10-100 km)—which is the dominant energetic scale in the ocean (Stammer, 1997) - and limits the model fidelity in coastal regions that are important areas of human activity, accounting for >80% of global fish catch (K. Sherman et al., 2009). Moreover, mesoscale features can be hotspots of biological activity, for example, by concentrating nutrients along fronts or eddies which can shift planktonic communities and lead to more efficient ecosystem transfer efficiency (Godø et al., 2012; Mahadevan et al., 2012; McGillicuddy, 2016; Woodson & Litvin, 2015). Thus, simulating the ocean at resolutions that permit coastal and mesoscale dynamics is desirable for many applications.

In this study, we introduce a new global high-resolution (nominal 0.1° horizontal resolution) ocean and sea ice simulation using the Community Earth System Model (CESM; Danabasoglu et al., 2020). The model is forced by the JRA55-do atmospheric state and runoff dataset over the period 1958 to 2021 (Kobayashi et al., 2015; Tsujino et al., 2020). The simulation employs the **Mar**ine **B**iogeochemical **L**ibrary (MARBL; Long et al., 2021) with a novel planktonic ecosystem that includes an explicit mesozooplankton group, thereby providing a food resource to higher trophic levels. In addition to presenting results from CESM, another major goal of this simulation was to enable offline simulation of fish. We used the the Fisheries Size and Functional Type (FEISTY) model to simulate higher trophic levels (Petrik et al., 2019). The FEISTY model is a size- and trait-based model that resolves the structure of fish communities from environmental forcing, i.e., mesozooplankton biomass, temperature, and detritus flux to the seafloor. In the present configuration, FEISTY is run offline, forced by the high-resolution CESM model output; in the future, it will be an online component of CESM, as in Dupont et al. (2023).

In addition to documenting the offline coupling of FEISTY to CESM, we also evaluate this high-resolution simulation with respect to available observations, focusing in particular on elements of the solution pertinent to ocean biogeochemistry and marine ecosystems. We present analyses that highlight the influence of model resolution, ocean acidification over the 64-year reconstruction, the factors governing biogeography of trophic energy transfer, oxygen distributions, and fish biomass estimates from FEISTY. The overarching objectives of this integration are to 1) provide a reconstruction of the ocean's physical and biogeochemical state over the last several decades; 2) create initial conditions

for high-resolution, retrospective multi-annual forecast integrations with the full ESM (Chang et al., 2020; Yeager et al., 2023), enabling assessment of predictability characteristics of various elements of the Earth system, inclusive of an active ocean biogeochemistry model; and 3) serve as a baseline for comparison to a two-way, online coupled FEISTY-CESM simulation.

This paper is organized as follows. In section 2 we present the configuration details of our numerical experiments and describe the novel planktonic ecosystem in MARBL; section 3 focuses on model evaluation, providing comparisons to observations to evaluate the model skill of CESM and FEISTY in simulating global biogeochemistry and marine ecosystems, including a comparison of FEISTY fish catch to observed fish catches. Section 4 provides an overview of the model solution, offering preliminary analysis of large-scale to mesoscale ecosystem processes, from plankton to fish. Lastly, in Section 5 we summarize our findings and identify areas for future work.

2 Methods

2.1 CESM-MARBL configuration

We use the ocean and sea-ice components of CESM version 2.2 (Danabasoglu et al., 2020). The ocean component is the Parallel Ocean Program version 2 (POP2; Danabasoglu et al., 2012; Smith et al., 2010) and the sea-ice component is the CICE version 5.1.2 (CICE5; Hunke et al., 2015). We perform two forced ocean – sea-ice (FOSI) simulations integrated over the 1958–2021 period using the JRA55-do atmospheric state and runoff dataset (JRA55-do; Tsujino et al., 2018). The primary difference between the two simulations is the change in model horizontal resolution: the high-resolution simulation (here after FOSI-HR) uses a nominal 0.1° horizontal resolution (the same grid as in Chang et al. (2020) and Harrison et al. (2018)), while the low-resolution simulation relies on the standard nominal 1° horizontal resolution (here after FOSI-LR). Additional details about the implementation and parameter settings used for FOSI-HR and FOSI-LR can be found in Chassignet et al. (2020). The main distinctions between the simulations presented in this manuscript and the ones discussed in Chassignet et al. (2020) are: (1) MARBL is enabled, and (2) additional tuning of the sea-ice as in described in Yeager et al. (2022); for further details on model setup see Section 6.

The FOSI-HR has ∼70x the number of grid cells as the FOSI-LR, and the time step is 1/38 the size, so the expectation is that the FOSI-HR requires roughly 2700x the computer resources as the FOSI-LR. CESM does not scale optimally, and different choices in how to balance model cost and model throughput for the two runs resulted in the FOSI-HR only using 1000x the computer resources of the FOSI-LR but taking almost 30x the time to complete the simulation.

To initialize these simulations, we performed multiple repeating 61-year cycles (1958 - 2018) of JRA55-do forcings. For FOSI-HR a combined 244-year ocean sea-ice spin up simulation (four cycle) at the nominal 0.1° resolution is used. For FOSI-LR the ocean-sea ice with MARBL turned on spinup was forced by five repeating 61-year cycles of JRA55-do (305-year) of simulation at the nominal 1° resolution). The January 1st restart at the end of the respective spin up simulations are used to initialize FOSI-HR and FOSI-LR. MARBL was not enabled in the high-resolution spin up due to the prohibitive cost associated with running a prognostic ocean biogeochemistry model at this resolution. The MARBL initial condition for FOSI-HR was obtained by interpolating the restart at the end of the low resolution spin up onto the 0.1° POP grid.

In addition to the heat, freshwater, and momentum fluxes obtained from JRA-do, MARBL requires additional forcings in these FOSI simulations. We used historical atmospheric CO_2 ramping over the period 1958 to 2021, but also enable "ALT-CO2" parallel carbonate chemistry system, which functions as if atmospheric CO_2 remains at preindustrial levels. This allows a clean disentanglement of anthropogenic and natural carbon in the ocean, as well as a clear ocean acidification signal resulting from anthropogenic carbon. Transient atmospheric nitrogen deposition, from a previous fully coupled CESM2 simulation, was prescribed (Danabasoglu et al., 2020). Riverine inputs of dissolved inorganic carbon, dissolved organic matter, alkalinity, and nutrients (N, P, Si, and Fe) were held constant at year 1900 values from the GlobalNews dataset (Mayorga et al., 2010).

While most variables in the FOSI-HR were written out at a monthly time step, we created higher frequency time averages for certain variables. For example, the variables needed to force FEISTY (see section 2.2) were output at a daily time step since 1980. Additional 5 day output for some variables starts at 2006.

MARBL (marbl-ecosys.github.io) is the ocean biogeochemistry/planktonic ecosystem component in CESM2 (Long et al., 2021). In the following section, we describe the new configuration of the CESM-MARBL planktonic ecosystem, which has four phytoplankton functional types (PFTs) and two zooplankton functional types (MARBL-4p2z; Fig. 1, left side). Parameters in this ecosystem configuration were tuned in the 1° resolution and then applied for both the FOSI-LR and FOSI-HR simulations described here.

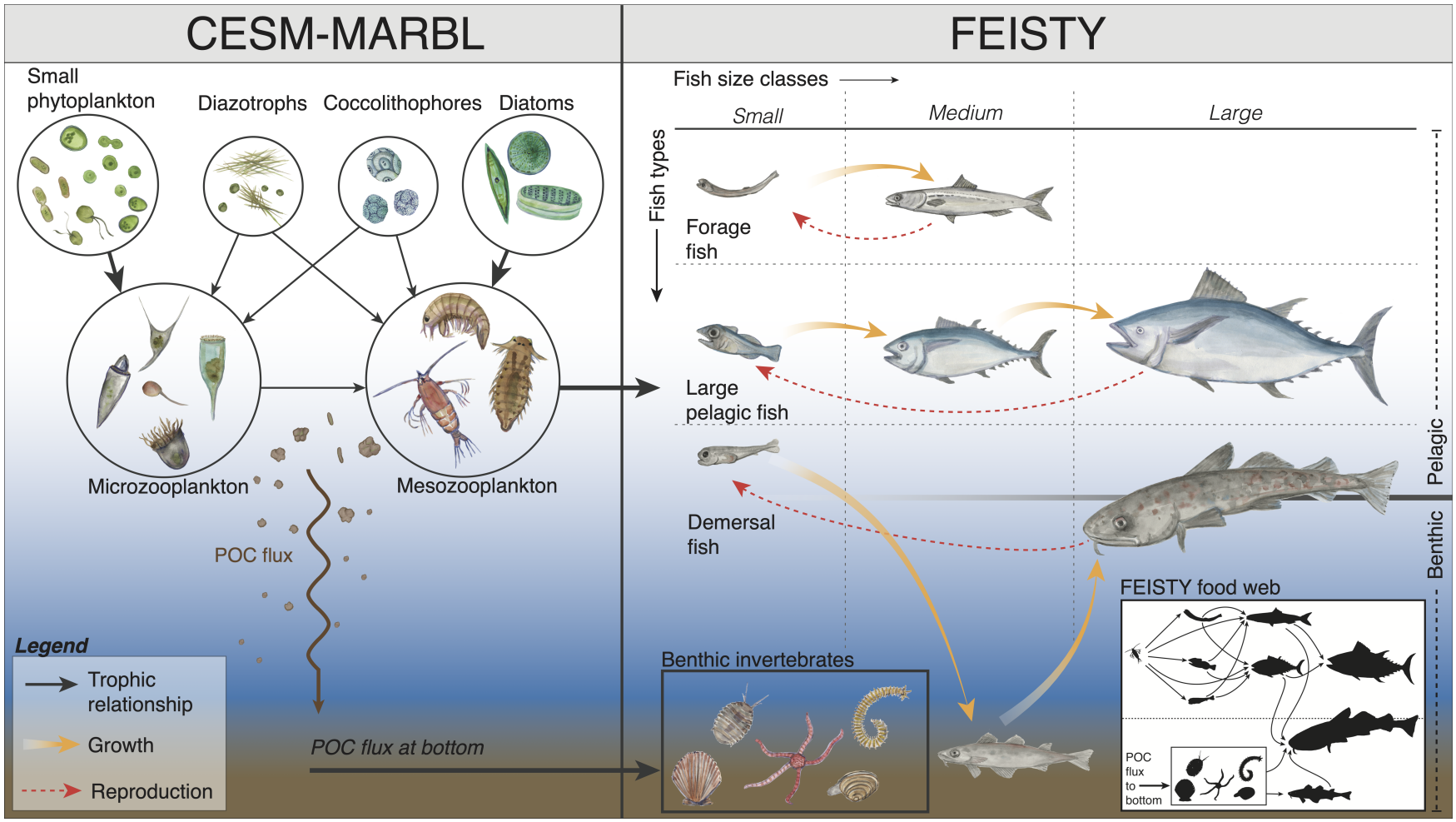

Figure 1: Connecting the CESM MARBL-4p2z planktonic ecosystem with the FEISTY fish model. The MARBL planktonic ecosystem configuration in CESM2 is shown on the left side, with illustrations of example organisms falling into each functional group. Grazing relationships implemented in the model are indicated by black arrows, with thicker arrows for small phytoplankton and diatom grazing because these comprise the bulk of global marine primary production in the model. A schematic of the FEISTY model (Petrik et al., 2019) is shown on the right side with yellow arrows indicating growth from one size class to the next and red dashed arrows indicating reproduction. FEISTY food web relationships are shown in the lower right corner. Abbreviations: particulate organic carbon (POC).

Table 1: List of relevant phytoplankton parameterizations used in MARBL-4p2z ecosystem. Abbreviations: Small phytoplankton (SP), diatoms (Diat), diazotrophs (Diaz), coccolithophores (Cocco), dissolved organic phosphorus (DOP).

Parameter	Unit	Definition	Cocco	Diat	SP	Diaz
μ_{ref}	d^{-1}	Max. C-specific growth rate	4.7	5.3	4.8	1.6
α	$\frac{mmolCm^2}{mgChlWs}$	Initial slope of photosynthesis-irradiance curve	0.31	0.39	0.35	0.31
Θ_{max}	$\frac{mgChl}{mmolN}$	Maximum Chl:N ratio	3.8	4.0	2.5	2.5
K_{Fe}	$\mu mol\ m^{-3}$	Fe half saturation constant	0.032	0.05	0.03	0.045
K_{PO4}	$mmol\ m^{-3}$	PO_4 half saturation constant	0.006	0.05	0.01	0.015
K_{DOP}	$mmol\ m^{-3}$	DOP half saturation constant	0.25	0.5	0.3	0.075
K_{NO3}	$mmol\ m^{-3}$	NO_3 half saturation constant	0.41	0.4	0.2	2
K_{NH4}	$mmol\ m^{-3}$	NH_4 half saturation constant	0.01	0.05	0.01	0.2
K_{SiO3}	$mmol\ m^{-3}$	SiO_3 half saturation constant	n/a	1.6	n/a	n/a
K_{CO2}	$mmol\ m^{-3}$	CO_2 half saturation constant	1	n/a	n/a	n/a
$mort$	d^{-1}	Linear mortality rate	0.1	0.1	0.1	0.1
$mort2$	d^{-1}	Non-linear aggregation rate	0.01	0.01	0.01	0.01

2.1.1 Phytoplankton in MARBL

Phytoplankton types are similar to previous versions of MARBL documented in Krumhardt et al. (2019) and Krumhardt et al. (2020): small phytoplankton (SP), diatoms, diazotrophs, and coccolithophores. Briefly, SP and diatom PFTs comprise the bulk of phytoplankton productivity, with diatoms dominating in nutrient-rich, light-limited regimes and SP thriving in nutrient-limited regions. The diazotroph PFT represents nitrogen-fixing phytoplankton, limited to areas warmer than 15°C. The coccolithophore PFT forms summertime blooms in high latitude, temperate regions, with a low level presence in low latitude regions. Its calcification is dependent on aqueous CO_2 concentration, nutrient limitation, and temperature (Krumhardt et al., 2020; Krumhardt et al., 2019).

All phytoplankton growth equations in MARBL are described in Long et al. (2021). Here, we briefly report the phytoplankton growth parameters associated with the planktonic ecosystem in this new, slightly more complex version (see Table 1). Phytoplankton growth rates (μ) are parameterized as the product of the resource-unlimited growth rate (μ_{ref}) at a reference temperature (30°C) and fractional limitation terms. Diatoms have the fastest μ_{ref}, while diazotrophs have the slowest μ_{ref} (Table 1). μ_{ref} is scaled by temperature, nutrient, and irradiance limitation terms. Diatoms, SP, and diazotrophs have the same temperature limitation function (T_f), parameterized as a Q10 temperature limitation function:

$$T_f = 1.7^{\left(\frac{T-30^\circ C}{10^\circ C}\right)}, \tag{1}$$

the parameters of which are based on results from E. Sherman et al. (2016). The coccolithophore PFT temperature limitation curve is a power function (Fielding, 2013; Krumhardt et al., 2017) and is less sensitive than the Q10 function to increases in temperatures higher than ~15° C. Light limitation (I_{lim}) of phytoplankton is follows Geider et al. (1997), using the values for the initial slope of the photosynthesis-irradiance curve (α) and the maximum chlorophyll to nitrogen ratio (Θ_{max}) reported in Table 1. Nutrient limitation is represented via Michaelis-Menten uptake kinetics, with nutrient half saturation constants reported in Table 1; aqueous CO_2 concentration may also limit coccolithophore growth via a half saturation constant for CO_2 (K_{CO2}), as described in Krumhardt et al. (2019) and Krumhardt et al. (2017).

Phytoplankton losses include a linear mortality rate representing cell death, a non-linear (density dependent) aggregation rate, and grazing by zooplankton. Mortality and aggregation rates and formulas are shown in Long et al. (2021) (rates listed in Table 1), while zooplankton grazing is described in the following paragraphs.

Table 2: List of relevant zooplankton parameters used in MARBL-4p2z ecosystem. Abbreviations: reference temperature (T_{ref}, 30°C), and maximum grazing rate ($g_{\max}$).

Parameter	Unit	Definition	Microzooplankton	Mesozooplankton
Maximum grazing rate	d^{-1}	sum of $g_{\max}$ of all prey at T_{ref}	6.8	1.615
GGE	fraction	Gross growth efficiency	0.25 – 0.35	0.25
K_P	$mmol/m^3$	Range of half saturation constants for prey	1.2 – 1.5	1 – 1.4
mort	d^{-1}	Linear mortality rate at T_{ref}	0.1	0.035
*mort*2	d^{-1} / $(mmol/m^3)$	Non-linear, density dependent mortality rate at T_{ref}	0.0028	0.020

2.1.2 Zooplankton in MARBL

Two broad zooplankton functional groups, nominally "microzooplankton" and "mesozooplankton", graze on the PFTs. The zooplankton groups are divided according to their size (though size - and parameters based on size - are not explicitly represented in MARBL-4p2z), mortality rate (i.e., lifespan or turnover time), and feeding preferences. While we provide some examples of what species these groups could represent (e.g., see Figure 1, left side), these are not meant to be specifically describing any particular zooplankton species in great detail. Because this is a global model, what species each zooplankton group represents would depend on geographic location; for instance, the mesozooplankton group could represent both Antarctic krill and copepods in the Southern Ocean.

General zooplankton parameters are shown in Table 2. Gross growth efficiency (GGE), the ratio of growth over ingestion (Welch, 1968), is highest at 0.35 for microzooplankton grazing on SP or diazotrophs. GGE is 0.25 for microzooplankton grazing on coccolithophores, reflecting reduced nutrition from a calcium carbonate-protected cell (Haunost et al., 2021). Mesozooplankton have a GGE of 0.25 for all prey. These GGE values are all within the range of observations (Straile, 1997). The maximum grazing rate (Tables 2 and 3) is higher for microzooplankton than mesozooplankton, and therefore decreases as zooplankton size increases, in line with observations (Hansen et al., 1997). Linear mortality rates (*mort*) reflect metabolic losses, as well as zooplankton longevity, with faster mortality rates for shorter–lived (smaller) zooplankton groups. A non-linear, density dependent mortality term (*mort*2) represents predation by organisms not explicitly simulated in the model; therefore, the mesozooplankton group has a higher *mort*2 than microzooplankton because it is not preyed upon by the other (larger) zooplankton in CESM (Table 2). Zooplankton grazing and mortality rates are scaled by the same Q10 function as for phytoplankton above (Equation 1).

2.1.3 Planktonic grazing relationships in MARBL

Grazing relationships are indicated in Figure 1, as well as in Table 3. The microzooplankton group has a diverse diet consisting of SP (e.g., *Prochlorococcus* and *Synechococcus*; Bemal and Anil (2019)), diazotrophs (e.g., small, unicellular diazotrophs; Wang et al. (2019)), and coccolithophores (small coccolithophores, such as *E. huxleyi*). Grazing of small phytoplankton by microzooplankton follows a Holling Type III relationship following findings of Bemal and Anil (2019) who showed that grazing on picophytoplankton follows this type of relationship:

$$G = g_{\max} \cdot T_{\text{lim}} \cdot Z \cdot \left(\frac{P^2}{P^2 + {K_{\text{P}}}^2} \right), \tag{2}$$

where $g_{\max}$ is the maximum grazing rate of microzooplankton (Table 3), T_{lim} is the same Q10 function as described above for phytoplankton temperature limitation (Equation 1), Z is the microzooplankton concentration, P is the small phytoplankton concentration, and K_P is the half-saturation constant for grazing for this relationship (see Table 3). All the other grazing relationships in this MARBL configuration are Holling type II, as shown in Long et al. (2021).

The mesozooplankton diet in the model consists primarily of diatoms, reflecting observations that diatoms serve as the dominant food source for copepods (Irigoien et al., 2002). The mesozooplankton group also grazes on coccolithophores (e.g., larger coccolithophores such as *Coccolithus pelagicus*),

Table 3: Maximum grazing rates ($g_{\max}$; d^{-1}) and half saturation constants for grazing (K_P; mmol m^{-3}) for each grazer-prey relationship in the MARBL-4p2z. Abbreviations: Small phytoplankton (SP), diatoms (Diat), diazotrophs (Diaz), coccolithophores (Cocco), microzooplankton (Microzoo), mesozooplankton (Mesozoo)

	Prey items									
	SP		**Diaz**		**Cocco**		**Diat**		**Microzoo**	
Grazers ↓	K_P	$g_{\max}$	K_P	$g_{\max}$	K_P	$g_{\max}$	K_P	$g_{\max}$	K_P	$g_{\max}$
microzoo	1.4	4.1	1.2	1	1.5	1.7	–	–	–	–
mesozoo	–	–	1.2	0.5	1.4	0.015	1.0	0.9	1.3	0.2

diazotrophs (e.g., larger N-fixing phytoplankton such as *Trichodesmium*), and microzooplankton. Diatoms have lower overall grazing rates than other phytoplankton in the model due to opal shell/spines protection from grazing, e.g., see Smetacek et al. (2002). Coccolithophores and diazotrophs are grazed by both microzooplankton and mesozooplankton, reflecting the wide size range of both of these groups (Balch, 2018; Nejstgaard et al., 1997).

2.2 Offline coupling of CESM to FEISTY

The FEISTY model was run in an "offline" fashion using output from the FOSI-HR and FOSI-LR simulations; results from the FEISTY simulations are referred hereinafter to as "FEISTY-HR" and "FEISTY-LR" for the FOSI-HR and FOSI-LR, respectively. In this context, "offline" means that CESM and FEISTY are only coupled in one direction (from CESM to FEISTY), and there is no feedback from fish on zooplankton or biogeochemistry in CESM. The CESM variables used to force FEISTY are pelagic temperature (top 150 m mean), mesozooplankton biomass and mesozooplankton loss rate (top 150 m depth integral), particulate organic carbon flux at the ocean floor, and temperature at the ocean floor (Petrik et al., 2019). At a given time step, fish encounter mesozooplankton biomass, but consumption rates of mesozooplankton are constrained to not exceed the predation mortality loss rates in the biogeochemical model. As the predation mortality loss rates were not saved as outputs from FOSI-HR, we used the total mortality loss rates for this constraint. All physiological rates in FEISTY (encounter, maximum consumption, basal metabolism) are temperature dependent following an Eppley curve. Encounter and maximum consumption rates have a Q10 of 1.88 while basal metabolism has a Q10 of 2.35Petrik:2019. These FEISTY forcing variables are output at a daily frequency from 1980 to 2021 and were used to force FEISTY at a daily time resolution; we note that this represents an improvement from previous FEISTY studies, where the forcing was monthly ESM output (Petrik et al., 2019; Petrik et al., 2020). We spun up the FEISTY model by repeating FOSI-HR and FOSI-LR year 1980 forcing one hundred times. In order to run FEISTY with daily forcings on the FOSI-HR grid, we have rewritten the MATLAB code used in Petrik et al. (2019) in Python (see section 6). The Python version allows parallel computations for FEISTY integration, thanks to thriving scientific Python ecosystem, and more specifically to the Xarray and Dask python libraries.

Here, we summarize the FEISTY model from Petrik et al. (2019). FEISTY simulates three fish functional types subdivided into several size classes (Figure 1, right side). The fish functional groups differ by their feeding and size niches. Forage fish are small pelagic fishes with small (larval) and medium (adult) size classes in FEISTY. Forage fish serve as prey for many marine animals and feed exclusively on zooplankton; examples include sardines, herring, and anchovies. Large pelagic fish coexist with forage fish in the upper water column and are characterized by a large adult size. FEISTY resolves three size classes of large pelagic fish: small (larval), medium (juvenile), and large (adult). Examples include tuna and mackerel. Lastly, demersal fish are generalist feeders that can feed on benthic resources, as well as pelagic resources in shallow shelf environments. Particulate organic carbon flux to the seafloor serves as a food resource for benthic invertebrates (Figure 1), which are consumed by juvenile and adult demersal fish. Larval demersal fish begin life in the pelagic realm and migrate to the seafloor as juveniles. Adult demersal fish can feed in both pelagic and benthic oceanic habitats in continental shelf regions <200 m. Examples of demersal fish include cod and flounder. The size structure, i.e., that individuals grow from the offspring size to the adult size, is a key aspect of the FEISTY model, as it determines most physiological processes, such as predation, mortality, and allocation of energy to growth and reproduction (K. H. Andersen et al., 2009; K. Andersen, 2019;

Olsson & Gislason, 2016).

2.3 Evaluation datasets

In this study, we focus on evaluating biogeochemical and ecosystem variables from the FOSI-HR. However, we acknowledge that physical variables, such as sea temperature and mixed layer depth, strongly impact biology. These fields have previously been evaluated for JRA-forced CESM2 integrations (see Small et al., 2024; Treguier et al., 2023), but sea ice has not. As sea ice is an important control on biological productivity in Arctic and Antarctic regions (Arrigo et al., 2008), we use sea ice index from the National Snow and Ice Data Center NSIDC; Fetterer et al., 2017 to evaluate modeled sea ice concentrations in FOSI-HR and FOSI-LR.

We use a variety of global biogeochemical metrics to evaluate the large scale biogeochemistry in FOSI-HR and FOSI-LR model solutions. These include globally-integrated NPP (Behrenfeld et al., 2005; Behrenfeld & Falkowski, 1997; Carr et al., 2006), particulate organic carbon (POC) export at 100 m (DeVries & Weber, 2017), diatom production and silicification (Holzer et al., 2014; Nelson et al., 1995), nitrogen fixation (Wang et al., 2019), and calcification (Liang et al., 2023; Ziveri et al., 2023, and references therein). For global scale zooplankton biomass and productivity, we use estimates of global microzooplankton and mesozooplankton biomass reported in Moriarty and O'Brien (2013) and Buitenhuis et al. (2010).

We use several spatially-resolved observation-based datasets to evaluate CESM model performance on a global scale. Modeled global macronutrient distributions, averaged over the period 1997 to 2017, are compared to World Ocean Atlas version 2 (Garcia et al., 2018), interpolated vertically and horizontally onto the model grids. We compare surface nutrients (top 10 m) and nutrients roughly below the thermocline (defined as 461.8 m to 503.7 m). We use the gridded monthly GOBAI-O2 product (2004–2021; Sharp et al., 2022) to validate oxygen distributions in both FOSI-LR and FOSI-HR . Modeled chlorophyll concentrations are compared to the GlobColour merged chlorophyll product, which incorporates NASA remote sensing observations from the Sea-viewing Wide Field-of-view Sensor (SeaWiFS), MODIS Aqua, and VIIRS satellite remote sensing platforms (Garnesson et al., 2019). The Coastal and Oceanic Plankton Ecology, Production, and Observation Database (COPEPOD) is used to evaluate the mesozooplankton biomass field in our simulations (Moriarty & O'Brien, 2013); we compare the 200-m mean mesozooplankton biomass estimates from COPEPOD to 150-m mean mesozooplankton biomass estimates from the model.

We employ the Sea Around Us (SAU) fish catch dataset to tune and validate the fish catch estimates in Large Marine Ecosystems (LMEs; Pauly et al., 2020), following Petrik et al. (2019) and Stock et al. (2017). Simulated "catches" in FEISTY are calculated by multiplying each fish functional group biomass by the fishing mortality rate. For simplicity, the fishing mortality rate is held constant at 0.3 yr^{-1} at all grid points, assuming constant fishing effort. The fished biomass is removed from the fish population at each timestep. We classify the fish functional groups from the SAU dataset into the three fish functional types in FEISTY following Petrik et al. (2019) and calculate area-weighted average catches for each LME. We only use 45 out of the 66 total LMEs, eliminating outliers that had low fishing effort and low catch, as in Stock et al. (2017) and Petrik et al. (2019). Further, we use the mean of the top 10 fish SAU catches for each LME in order to best represent potential fish catches, as discussed in Stock et al. (2017). We compare this processed SAU catch data to the mean of the FEISTY catch data over the 1980-2010 period. This time period was chosen because the SAU catch data that we used here spans from 1950-2010 while the FEISTY catch data spans from 1980-2021, so 1980-2010 is the overlap between the two datasets. We used the same SAU data that was used in the FEISTY description paper (Petrik et al., 2019). We compute correlation coefficients that characterize the mean spatial fidelity of the modeled fish catches (mean modeled catch versus mean observed SAU catch in each LME), as well as correlations in fish catch over time for certain highly fished LMEs (e.g., the California Current) to evaluate temporal variability in fish catch.

2.4 Analysis

In many of the figures in this study, we show snapshots from the FOSI-HR and FEISTY-HR in order to highlight mesoscale features. We aimed to capture different regions of the ocean with various ecological characteristics (e.g., upwelling versus subtropical, warm versus cold). The choice of the timing of the snapshots we show is rather arbitrary; however, we chose points within the growing season in temperate

and polar regions to showcase the ecological dynamics when they are most active. We contextualize each snapshot, referencing to Figure S1, which shows time series of sea surface temperature, net primary productivity, and total fish biomass for each region shown in the figures presented in this study.

3 Evaluation of ecosystem-related fields

From a global perspective, ecosystem and biogeochemistry metrics calculated for FOSI-HR and FOSI-LR are similar to observation-based metrics (Table 4). Globally-integrated marine NPP in both FOSI-HR and FOSI-LR falls within the range of observation-based estimates at ∼52 Pg C yr^{-1}, with about 38% (40%) of that production coming from diatoms for FOSI-HR (FOSI-LR). Approximately 12% (13%) of NPP, 6.39 Pg C yr^{-1} (6.73), is exported below 100m (POC export 100m; Table 4) in the FOSI-HR (FOSI-LR). Net globally-integrated silicification within the top 100m is on the low end of observation-based estimates at just above 100 Tmol of Si yr^{-1} for both simulations. The diazotroph phytoplankton type in the model fixes approximately 176 Tg N yr^{-1} in FOSI-HR, which falls into the plausible range estimated using an inverse model by Wang et al. (2019). Observation-based estimates of globally-integrated calcification vary greatly, between 0.7 and 4.7 Pg C yr^{-1}, with much of the discrepancy likely due to uncertainty regarding the potentially large portion of biogenic $CaCO_3$ remineralized in the photic zone (Ziveri et al., 2023). In the FOSI-HR, the coccolithophore PFT produces 0.87 Pg C yr^{-1} (net calcification) in the top 100 m; FOSI-LR calcification is just slightly higher at 0.90 Pg C yr^{-1}.

While there are large uncertainties associated with global inventories of zooplankton biomass, we do provide a comparison to previously published estimates for microzooplankton and mesozooplankton, the two zooplankton groups in FOSI-HR. Buitenhuis et al. (2010) estimated a global microzooplankton biomass inventory of between 0.14 to 0.33 Pg C and the FOSI-HR microzooplankton falls within this range at 0.24 Pg C. While observation-based estimates of mesozooplankton biomass are similar to microzooplankton at 0.19 Pg C, FOSI-HR has a substantially higher mean global inventory of 0.38 Pg C of mesozooplankton biomass. Though an uncertainty range was not provided in Moriarty and O'Brien (2013), the median biomass concentration on which the estimate is based is bounded by a large standard deviation (2.7 µg C L^{-1} ±10.6). Furthermore, the absence of an explicit macrozooplankton representation in MARBL could mean the mesozooplankton group may also represent macrozooplankton biomass. For example, the mesozooplankton group in MARBL consumes both diatoms and microzooplankton (Figure 1) and thus could also be representative of Antarctic krill which also consume these two groups (Haberman et al., 2003), but are not included in the observationally-based mesozooplankton biomass estimate (rather krill are classified as macrozooplankon). This could explain why FOSI-HR (and FOSI-LR) has more mesozooplankton biomass than the observation-based estimate from Moriarty and O'Brien (2013). As an addition zooplankton global metric, total zooplankton production (microzooplankton + mesozooplankton groups) should be at least 21% of globally integrated NPP (Landry and Calbet (2004) estimated that *only* microzooplankton production constitutes 21% of NPP); in FOSI-HR and FOSI-LR it is ∼25%. Furthermore, a recent study by Hatton et al. (2021) estimated global microzooplankton and mesozooplankton biomass by spatially interpolating the Moriarty and O'Brien (2013) and Buitenhuis et al. (2010) estimates along with other recent observations. The Hatton et al. (2021) estimates of 0.23 and 0.41 Pg C are remarkably close to the FOSI-HR estimates of 0.24 and 0.38 Pg C, respectively, assuming a 10% carbon to wet weight conversion ratio.

While there are not observations of total fish biomass in the ocean, we compare FEISTY-HR and FEISTY-LR to two recent modeling efforts to estimate fish biomass. Total fish biomass in FEISTY-HR and FEISTY-LR is 2.00 ± 0.04 and 2.26 ± 0.05, respectively. Jennings and Collingridge (2015) used a size-based macroecological model, estimating fish and total consumer biomass in the global ocean to be 4.9 Pg WW, with large uncertainty bounds (50% uncertainty intervals are 2 to 10.4 Pg WW). The model used in this study, however, considers much larger consumers (1 to 1000 kg) than FEISTY (0.02 to 5.6 kg), perhaps explaining some of the difference with FEISTY results. More recently. Bianchi et al. (2021) estimated global fish biomass using a data-constrained model, ranging between 4.7 ± 1.1 Pg WW (with fishing) and 6.9 ± 3.3 Pg WW (without fishing), falling within the range of the Jennings and Collingridge (2015) study, but somewhat higher than FEISTY results. While large uncertainties in estimating fish biomass, global FEISTY fish biomass is on the same order of magnitude as other published estimates. Interestingly, the FEISTY-LR has ∼13% more fish biomass than the FEISTY-

HR. Other than fish biomass, all of the metrics listed in Table 4 are very similar between the low- and high-resolution integrations, demonstrating consistency in large-scale CESM marine ecosystem characteristics regardless of resolution.

Table 4: Global biogeochemical metrics from the FOSI-HR, FOSI-LR, and observationally-derived estimates. For fish biomass from FEISTY-HR and FEISTY-LR, we compare to two previous fish/marine animal modeling efforts. FOSI and FEISTY metrics are averaged over the period 1986 to 2005. The "±" numbers behind the FOSI and FEISTY metrics represent standard deviation of interannual variability. Abbreviations: net primary productivity (NPP), particulate organic matter flux at 100m (POC export 100m).

Metric	**Unit**	**FOSI-HR**	**FOSI-LR**	**Observations**	**Reference**
Globally-integrated NPP	Pg C y^{-1}	52.26 ± 0.60	52.95 ± 0.60	43.5 to 67	Behrenfeld et al. (2005), Behrenfeld and Falkowski (1997), and Carr et al. (2006)
POC export 100m	Pg C y^{-1}	6.39 ± 0.13	6.73 ± 0.12	4 to 12	DeVries and Weber (2017)
% NPP by diatoms	%	38.17 ± 0.59	39.66 ± 0.54	40%	Nelson et al. (1995)
Net globally-integrated silicification within top 100 m	Tmol Si y^{-1}	101.73 ± 3.05	104.91 ± 2.94	100 to 140	Holzer et al. (2014) and Nelson et al. (1995)
Globally-integrated nitrogen fixation	Tg N y^{-1}	176.34 ± 2.18	169.83 ± 2.33	125.6 to 222.9	Wang et al. (2019)
Globally-integrated calcification	Pg C y^{-1}	0.87 ± 0.028	0.90 ± 0.012	0.7 to 4.7	Liang et al. (2023) and Ziveri et al. (2023) and refs therein
Microzooplankton biomass	Pg C	0.24 ± 0.00093	0.23 ± 0.00085	0.14 to 0.33	Buitenhuis et al. (2010)
Mesozooplankton biomass	Pg C	0.38 ± 0.0040	0.40 ± 0.0039	0.19	Moriarty and O'Brien (2013)
Zooplankton production % of NPP	%	25.35% ± 0.10	25.20 ± 0.082	at least 21%	Landry and Calbet (2004)
Total Fish/other consumers biomass	Pg WW	2.00 ± 0.04	2.26 ± 0.05	2 – 10.4	Bianchi et al. (2021) and Jennings and Collingridge (2015)

3.1 Sea ice

Sea ice impacts ecosystems both directly (e.g., as substrate for resting, hunting, breeding, protection from predators; and by limiting light availability for phytoplankton) and indirectly (e.g., sea ice and its seasonal cycle can impact ocean circulation, water column physics and chemistry, weather patterns, coastal erosion rates, etc.) in both Arctic and Antarctic marine environments (e.g., Deppeler & Davidson, 2017; Macias-Fauria & Post, 2018, and references therein). Adequate simulations of sea ice including seasonality, distributions, regionalities and trends - are critical for modeling of high latitude marine ecosystems and sea ice-related changes in marine ecosystems (e.g., Flores et al., 2023).

Sea ice concentrations (SICs) in FOSI-LR and FOSI-HR compare well, spatially and temporally, with National Snow and Ice Data Center (NSIDC) Climate Data Record (CDR; Meier et al., 2021) for both Arctic and Antarctic (Figure 2). Pattern correlations between observations and model output are slightly higher for the Arctic (R=0.95) than the Antarctic (R=0.92). Trends, interannual variability and climatological seasonal cycle for sea ice extent (SIE; defined as the area covered by sea ice concentrations of 15% or higher) from the NSIDC Sea Ice Index (Fetterer et al., 2017) are particularly well captured by the FOSI-HR simulation. Time series of annual sea ice extent are significantly correlated (at 98% based on a student-t test) for both LR and HR models and in both hemispheres, although correlations are higher for the Northern Hemisphere (NH) time series (R=0.98 for both FOSI-HR and FOSI-LR) than for the Southern Hemisphere (SH; R=0.75 for FOSI-HR and R=0.78 for FOSI-LR). Mean annual (1979—2020) SIE for FOSI-HR (11.3 x 10^6 km^2) and FOSI-LR (10.9 x 10^6 km^2) fall within one standard deviation of the observed NH annual SIE (11.3 $\pm$ 0.7 x 10^6 km^2), however in the SH the FOSI-HR (12.0 x 10^6 km^2) tends to overestimate SIE and FOSI-LR (10.7 x 10^6 km^2) tends to underestimate compared to the observations (11.5 $\pm$0.4 x 10^6 km^2). Both the FOSI-HR and FOSI-LR capture observed sea ice area means and temporal and spatially variability quite well compared to CMIP6 models in general (e.g., Roach et al., 2020). The FOSI-HR tends to better capture observed sea ice mean, seasonal cycle and variability than the FOSI-LR in the SH. The FOSI-LR tends to underestimate Antarctic and Arctic SIEs throughout the year. In short, we see a marked improvement in the high resolution simulation of sea ice in CESM. In turn, polar ecosystems, in which sea ice plays a substantial role, are likely to be better simulated in FOSI-HR as compared to the lower resolution version of CESM.

3.2 Oxygen distributions in the ocean

Oxygen concentrations are important for characterizing habitable parts of the ocean. Ocean oxygen distributions at various depths in the upper ocean in the FOSI-HR and FOSI-LR are compared to an observation-based gridded oxygen product (GOBAI-O2; Sharp et al., 2022) in Figure 3. At 100 m depth, oxygen concentrations in both high and low resolution CESM simulations match well with the geographic patterns of time-mean oxygen concentrations in the GOBAI-O2 product, except for some positive biases in low latitude regions. However, there are small regions where we observe a notable improvement in the FOSI-HR, as compared to the FOSI-LR. Spatial oxygen variability in coastal regions, such as the Gulf of Alaska, for example, in FOSI-HR match the GOBAI-O2 product better than the FOSI-LR. However, the low oxygen concentrations at 100 m depth in the northern Indian Ocean shown in the observation-based product are not fully captured in either CESM simulation. At 200 m depth, oxygen concentrations decline in equatorial regions and the North Pacific (Figure 3, middle column). The spatial patterns of this decline in oxygen are somewhat better captured in the FOSI-HR than the FOSI-LR, compared to the GOBAI-O2 product. Notably, oxygen at 200 m depth in the equatorial Atlantic declines too much in the FOSI-LR, while FOSI-HR better matches observations. FOSI-HR appears to resolve deep eastward equatorial jets that help oxygenate this region. Mesoscale eddies may also help ventilate equatorial regions, as shown by Eddebbar et al. (2021) using a similar high resolution CESM simulation. This is also evident at 400 m depth, where thin zonal strips of the equatorial regions have slightly higher oxygen than the FOSI-LR. Overall, however, FOSI-HR captures the expansive oxygen minimum zones at 400m seen the GOBAI-O2 product. Though the GOBAI-O2 product only extends down to 64.5°S, we also infer a notable improvement in oxygen concentrations in the FOSI-HR Southern Ocean at 200 m and 400 m as compared to the FOSI-LR, which has larger positive biases.

The widespread negative biases in oxygen at 400m seen in the FOSI-LR are not as prominent in the FOSI-HR (Figure 3n,o.) This suggests that some of the oxygen ventilation issues discussed in

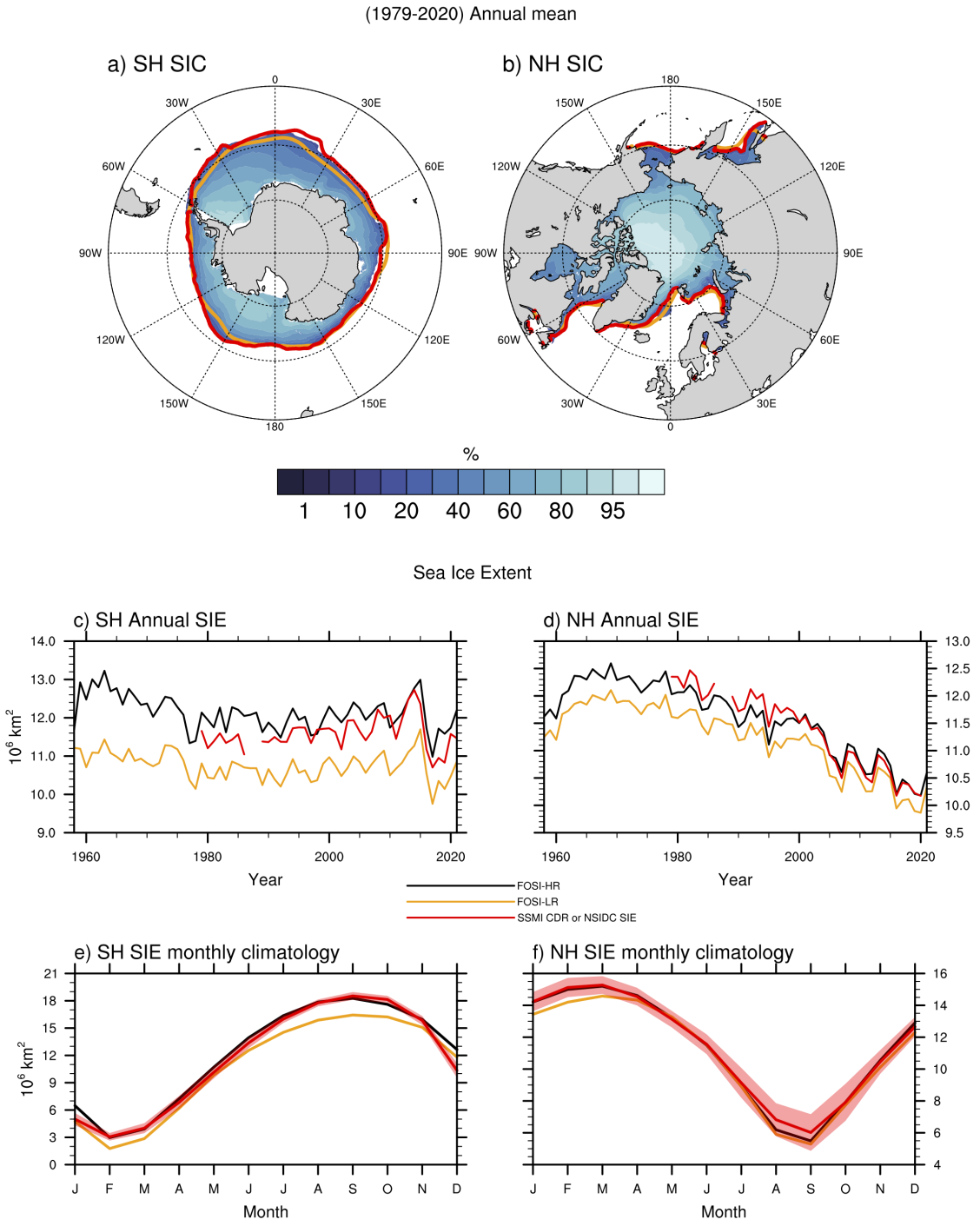

Figure 2: Annual mean sea ice concentrations (top), sea ice extent (SIE; middle) and climatological SIE seasonal cycle for Southern Hemisphere (left) and Northern Hemisphere (right) sea ice. Filled contours shown on maps in panels a and b are from FOSI-HR, with 15% sea ice concentration (SIC) for FOSI-LR (orange) and SSMI-Climate Data Record (red) overlain. Time-series and climatological cycle plots (panels c–f) show values for FOSI-HR (black), FOSI-LR (orange) and NSIDC SIE (red). Climatologies are calculated from 1979-2020. Red shading in the monthly climatology panels indicates mean observed SIE climatology ± 1 standard deviation. Observed SIE are from the National Snow and Ice Data Center (NSIDC) Sea Ice Index version 3.0 (Fetterer et al., 2017).

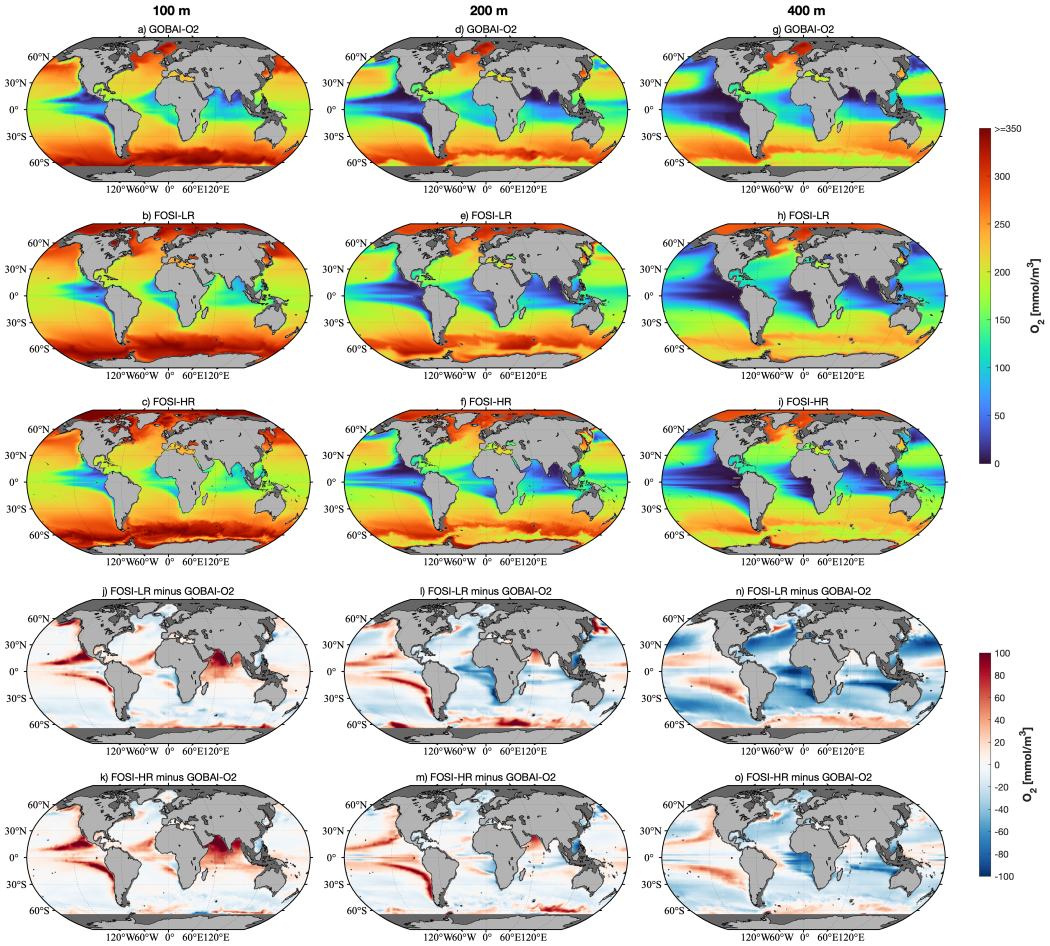

Figure 3: Time-mean (2004-2021) oxygen concentrations at depths of 100, 200, and 400 m for the gridded monthly observation-based GOBAI-O2 (Sharp et al., 2022) product (top row), the FOSI-LR (second row), and the FOSI-HR (middle row). Difference maps are shown between the GOBAI-O2 product and the FOSI-LR and FOSI-HR (bottom two rows) for each depth level.

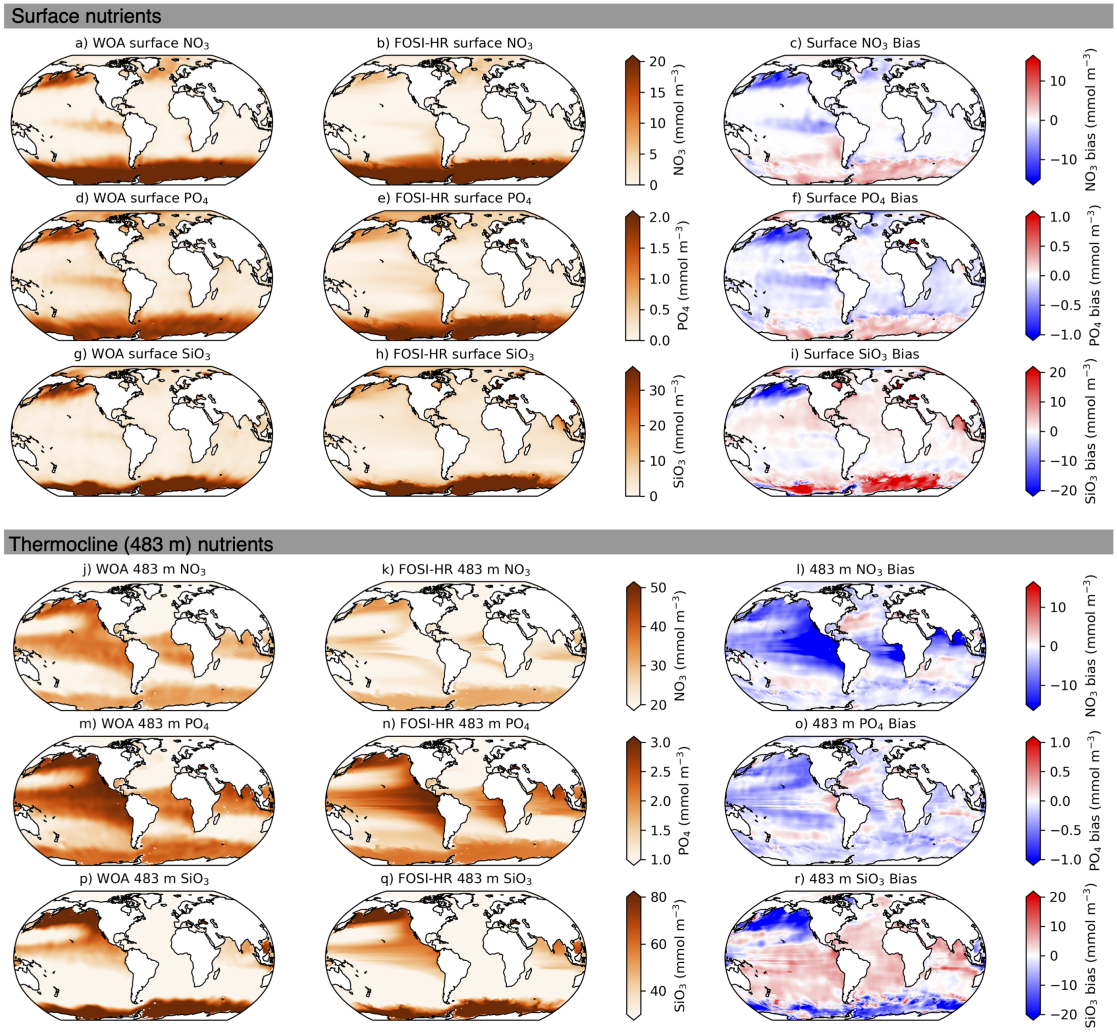

Figure 4: Comparison of FOSI-HR surface and thermocline (depth range between 461.8 m and 503.7 m) nutrients to World Ocean Atlas, v2 (WOA) (Garcia et al., 2018).

Long et al. (2021) may be improved using high resolution. Note that the expected improvement in equatorial ventilation from the higher resolution in FOSI-HR is not fully realized because the FOSI-HR simulation was initialized from a lower resolution spin up simulation where the ventilation biases had established overly extensive low oxygen zones at ∼400 m (see Methods).

3.3 Global distribution of nutrients

Global surface nutrient concentration distributions in the FOSI-HR match the World Ocean Atlas (WOA) well in most regions (Figure 4a–i; see Figure S2 for a FOSI-LR version of the figure). Surface nitrate (NO_3) and phosphate (PO_4) concentrations are low in low to mid-latitude regions and elevated in regions polewards of ∼45°. The FOSI-HR captures these overall patterns, except for some negative biases in the North Pacific, North Atlantic and equatorial Pacific. The global RMSE for surface NO_3 and PO_4 is 2.35 and 0.19 mmol m^{-2} and the spatial correlations are 0.96 and 0.95 ($p<0.001$), reflecting a good correspondence of spatial patterns in these macronutrients.

A slightly lower spatial correlation for surface SiO_3 in FOSI-HR (0.92; $p<0.01$), in contrast to NO_3 and PO_4, indicates more spatial biases. Surface silicate (SiO_3) matches well in low to midlatitudes and in the North Atlantic (Figure 4g–i). SiO_3 concentrations, however, are too low in FOSI-HR in the North Pacific where diatom growth (and hence SiO_3 drawdown) is perhaps too vigorous. We note that these negative nutrient biases in the North Pacific were also present in previous versions of CESM

(Long et al., 2021; Moore et al., 2013). In the Southern Ocean there are large swaths of too much surface SiO_3, as well as NO_3 and PO_4, where diatom growth may not be vigorous enough, perhaps overly limited by iron availability. Curiously, FOSI-LR has the opposite problem in the Southern Ocean – not enough SiO_3 at the surface relative to observations (Figure S2i). Overall, the global RMSE of SiO_3 is 6.31 mmol m^{-2}.

Deeper in the water column, around the thermocline at 483 m, nutrient biases in FOSI-HR change relative to the surface (Figure 4j–r; Figure S2 for the FOSI-LR version of the figure). While the overall geographical patterns match, there are some notable mismatches and RMSE for all nutrients increases with depth (NO_3 RMSE = 17.5; PO_4 RMSE = 1.37; SiO_3 RMSE = 31.24 mmol m^{-3}). NO_3 concentration biases are largely negative at this depth, especially in the Pacific Ocean. Some of this negative bias could be due to too much denitrification in the model within the oxygen minimum zones (section 3.2). PO_4 is also somewhat negatively biased globally around the thermocline, suggesting that more PO_4 should be remineralized higher in the water column. Spatial pattern correlations for NO_3 and PO_4 are lower than at the surface (0.50 and 0.34, respectively), but still statistically significant ($p < 0.001$). The bias patterns for NO_3 and PO_4 are substantially different for the FOSI-LR, where positive biases in the model manifest in mid-latitude regions (Figure S2, panels l and o). Lastly, SiO_3 concentrations are somewhat too high for much of the global ocean at 400 m in the FOSI-HR, except for the North Pacific and the Southern Ocean. In the North Pacific too much SiO_3 from overactive diatoms at the surface is being exported below 500 m causing a negative bias in the model. In the Southern Ocean, the positive SiO_3 bias at the surface (Figure 4i) switches to being negatively biased by 500 m, indicating that while there may not be enough diatom silicification at the surface, what is being produced is being exported too deep; these same biases are present in the thermocline for FOSI-LR (Figure S2). The spatial correlation is 0.71 at 483 m for SiO_3.

3.4 Global distribution of plankton

Global spatial patterns of surface chlorophyll match well between satellite observations and FOSI-HR simulation (Figure 5a,b; see Figure S3 for a FOSI-LR version of the figure; spatial correlation = 0.38). The chlorophyll maps presented in Figure 5a and b show elevated chlorophyll in the high latitudes (>45°), with lower concentrations in the subtropical gyres, for both FOSI-HR and the NASA satellite merged product (Garnesson et al., 2019). Chlorophyll is too elevated, however, for the equatorial Pacific and subantarctic Southern Ocean in FOSI-HR. By contrast, chlorophyll concentrations in the Arctic and Antarctic sea ice zones is generally underestimated in FOSI-HR according to this comparison. However, the satellite observations of chlorophyll in high latitude regions are only averaged over polar day, when expansive phytoplankton blooms are underway, and enough light and low sea ice allow ocean color retrieval. Therefore, we expect "annual average" chlorophyll observations in polar regions to be higher than the annual averages in the model, which averages over all months of the year. Overall, global chlorophyll RMSE is 0.51 mg m^{-3}.

The COPEPOD database (Moriarty & O'Brien, 2013) provides mean top 200 m concentration of mesozooplankton biomass, particularly copepods, which we compare to top 150 m mean biomass of the mesozooplankton functional type (see Figure 1) from the FOSI-HR (only the top 150 m of ecosystem variables are written out by the model). Like chlorophyll, the global spatial patterns of mesozooplankton biomass are similar between the observations and the model (Figure 5c,d; Figure S3c,d; spatial correlation = 0.41). Though the COPEPOD database is lacking coverage in the subantarctic part of the Southern Ocean, the data points that are present suggest an overestimation of mesozooplankton biomass in this region in the model. The extremely high mesozooplankton biomass seen in the COPEPOD dataset in the North Pacific is only partially captured by FOSI-HR. Global RMSE for the FOSI-HR compared to the COPEPOD dataset is 10.6 mmol m^{-3}.

3.5 Spatial and temporal variability in NPP

To evaluate FOSI-HR representation of mean state and temporal variability of marine ecosystems, we compare 150 m depth-integrated NPP from the model to satellite-derived NPP (Figure 6; see also Figure S4 for a FOSI-LR version of the figure). As different algorithms for estimating NPP from ocean color data can vary substantially with respect to spatial patterns and magnitudes (Saba et al., 2011), we compare NPP from FOSI-HR to two different algorithms: the Vertically Generalized Production Model (VGPM; Behrenfeld & Falkowski, 1997) and the Carbon-based Productivity model (CbPM;

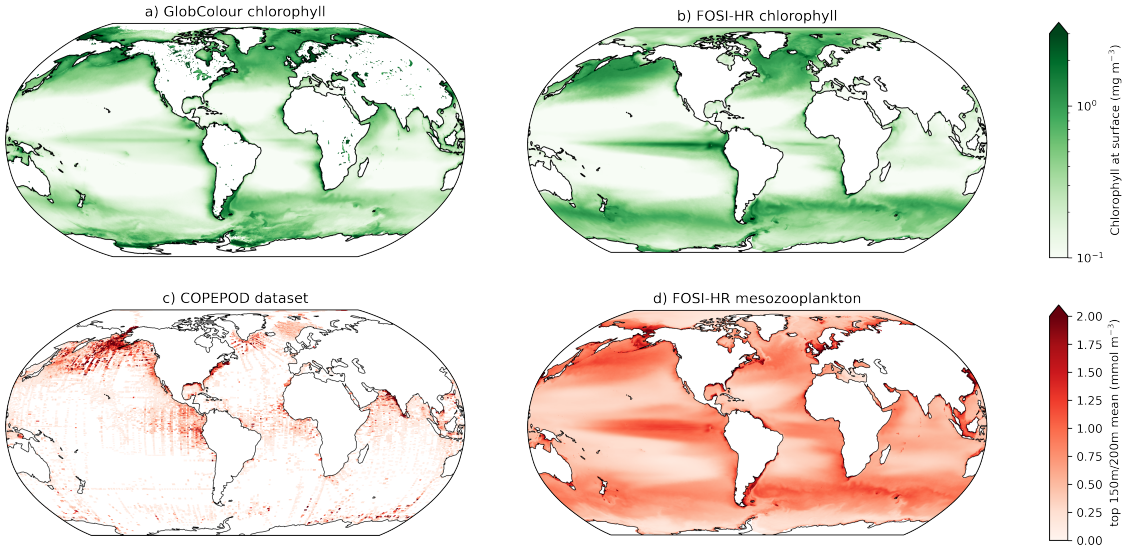

Figure 5: FOSI-HR chlorophyll comparison to GlobColour merged product (SeaWiFS, MODIS, VIIRS) and mesozooplankton/COPEPOD comparison (Garnesson et al., 2019). The chlorophyll observations and FOSI-HR chlorophyll are a mean over 1997 to 2021. Mesozooplankton biomass from FOSI-HR is averaged over the same time period, 1997 to 2021, and we compare that to the to the COPEPOD database, which is a compilation of mesozooplankton biomass measurements starting as early as 1951 (Moriarty & O'Brien, 2013).

Behrenfeld et al., 2005; Westberry et al., 2008). Both algorithms tend to have more concentrated NPP along coastal regions, as compared to the FOSI-HR. However, the VGPM has very low NPP in the oligotrophic gyres (Figure 6a), while the CbPM algorithm captures higher NPP in open ocean regions and productivity is spread out further from the coast (Figure 6b). Mean FOSI-HR NPP matches better to the CbPM oligotrophic gyres, even though the modeled NPP is slightly higher than CbPM. FOSI-HR is substantially higher than both NPP algorithms in the equatorial Pacific (Figure 6c) This is also true for FOSI-LR (Figure S4c). On the other hand, NPP in FOSI-HR is somewhat too low in polar regions, as compared to both observation-based estimates. For some regions, such as the northern Indian Ocean, FOSI-HR NPP falls between VGPM and CbPM. Overall large scale geographic patterns in ocean NPP match well between FOSI-HR and satellite-based estimates (Figure 6a–c). The spatial pattern correlation between FOSI-HR NPP and CbPM is higher (0.41) than the correlation between FOSI-HR and the VGPM (0.24); similarly the RMSE for FOSI-HR is higher when compared to VGPM (428.1 mg C m^{-2} d^{-1}) than to CbPM (275.0 mg C m^{-2} d^{-1}).

In order to examine how well NPP variability is captured in the FOSI-HR, we consider regional averages of ocean NPP in three regions representing a variety of oceanographic environments: the equatorial Pacific, subtropical Atlantic, and the Indian sector of the subantarctic Southern Ocean (Figure 6d–f). Thus, we aim to evaluate NPP in a tropical, high productivity region, a subtropical gyre, and a subpolar area of vigorous mesoscale activity, all subject to different limitations and drivers of NPP. We created anomalies to compare the interannual variabilty in NPP in each region. Overall FOSI-HR matches the VGPM better in terms of NPP variability than the CbPM, as all regional correlation coefficients are above 0.5 and statistically significant ($p < 0.05$); this is also the case for FOSI-LR (Figure S4). CESM NPP is substantially higher than both satellite-derived estimates for the equatorial Pacific (905 mg C m^{-2} d^{-1}, compared to 616 and 353 from CbPM and VGPM, respectively); equatorial Pacific NPP in the FOSI-LR is 733 mg C m^{-2} d^{-1} (Figure S4d). However, the variability in NPP matches well in this region with both NPP algorithms, both showing significant correlations with FOSI-HR NPP, likely driven by a strong response to El Niño-Southern Oscillation (ENSO). For the subtropical North Atlantic, all three NPP anomaly time-series match well during the first half of the time-series, but post-2012 the time-series diverge. However, the overall magnitude of NPP for the nutrient-limited subtropical North Atlantic matches well for all the estimates (ranging from 257 to 330 mg C m^{-2} d^{-1}). The southwest Indian Ocean NPP is more uncertain and the CbPM NPP appears to

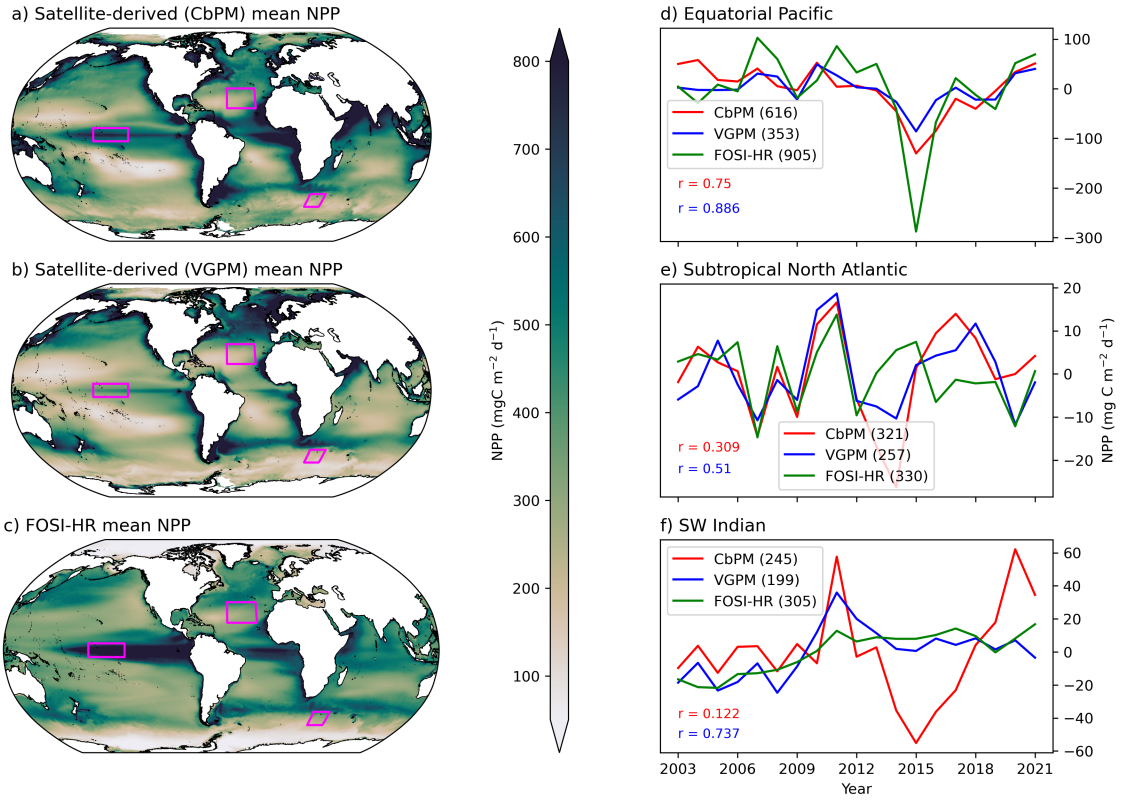

Figure 6: Mean net primary productivity (NPP) over the period 2003 to 2021 as estimated via the Vertically Generalized Production Model VGPM; Behrenfeld and Falkowski, 1997, the Carbon-based Productivity model CbPM; Behrenfeld et al., 2005; Westberry et al., 2008 and the FOSI-HR (panels a, b, and c, respectively). Time-series anomalies of NPP from the VGPM, CbPM, and the FOSI-HR plotted along the right-hand side are area-weighted means in the three boxes indicated on the maps (panels d–f). Correlation coefficients between FOSI-HR NPP and each observation-based estimate are indicated in each panel (CbPM in red and VGPM in blue). We use anomalies to compare variability, but the average magnitude of NPP varies for each region; we report the magnitudes of NPP for each boxed region in the legend (in mg C m^{-2} d^{-1}) for each region. The latitude and longitude boundaries for each region are as follows: Equatorial Pacific (5°S to 5°N and 165°W to 135°W), Subtropical North Atlantic (20°N to 35°N and 50°W to 25°W), and Southwest Indian(55°S to 45°S and 30°E to 45°E). See Figure S4 for a FOSI-LR version of this figure.

be the outlier with respect to interannual variability (Figure 6f). Overall, FOSI-HR NPP features low variability in the southwest Indian Ocean as compared to CbPM- and VGPM-based estimates. The differences could be due circulation biases or variability in mesoscale activity in the southwest Indian Ocean, where the Antarctic Circumpolar Current likely projects onto NPP.

3.6 Evaluating fish catch in Large Marine Ecosystems

We use SAU observations of fish catches (Pauly et al., 2020) in a subset of Large Marine Ecosystems (LMEs; see Methods section 2.3; see Figure S5 for the FOSI-LR version of this figure) to evaluate the simulation of fish in FEISTY subject to outputs from FOSI-HR. The top half of Figure 7 shows a mean state evaluation of fish catches in the FEISTY-HR, where each dot represents one of 45 LMEs included in the comparison (see Methods). In general, we observe a moderate match between the FEISTY and SAU datasets, which is in most cases slightly better for FOSI-HR than for FOSI-LR. We note a particularly positive correlation for demersal fish (r = 0.66), while forage fish are not correlated (r = -0.01), with SAU data showing a greater spread than FEISTY data. We note that Petrik et al. (2019) also report a lower correlation for forage fish with the SAU data than the other two fish functional types in FEISTY. Large pelagic fish match the SAU data moderately well (r = 0.35).

While it is challenging to pinpoint why one fish type would match the SAU data better than another, we speculate here on reasons for the mismatch but also refer readers to Petrik et al. (2019) for more details. For forage fish, it could be that there is substantial variation across LMEs in fishing effort of forage fish, which is not reflected in the constant fishing mortality applied in the simulations. It could also be that the forage fish functional type is representing a portion of mesopelagic fish biomass, which is not targeted by fisheries. Furthermore, the forage fish biomass is heavily influenced by predation by - and competition with - the large pelagic fish type in FEISTY, so biases in large pelagic fish will be propagated to forage fish. Possible reasons for biases in large pelagic fish include competition with marine mammals and sea birds in cooler oceanic environments, as well as lack of simulated fish movement, neither of which are represented in FEISTY. Not simulating movement for feeding or spawning by large pelagic fish could lead to an underestimate of biomass in the tropics and subtropics. Further analysis on biases in fish biomass with regard to the SAU data is beyond the scope of this manuscript, and could be a focus area for future research effort.

The bottom half of Figure 7 shows annual mean time-series for two LMEs: the California Current and the Southeast U.S. Continental Shelf. For the California Current LME, interannual variability is well-correlated between the two datasets, while the relationship is less pronounced for the Southeast U.S. Continental Shelf. Note the different axes used for FEISTY and SAU data; for both of these LMEs, FEISTY catch magnitudes are consistently higher than SAU catches. This disparity could be expected given that in FEISTY, fish catch is represented as a simple fraction of total fish biomass, while the SAU data is affected by many other factors like variability in fishing effort, which is influenced by human factors distinct from climate forcing alone. Nevertheless, the comparison in variability between these datasets is still meaningful despite the difference in magnitude.

4 Results

4.1 Large scale biogeography of plankton to fish

The high resolution simulations, FOSI-HR and FEISTY-HR, aim to link nutrients to fish on a global scale. While the fine scale details in this high-resolution global simulation are what make it truly unique, it is important to contextualize these details in a global overview. In Figure 8 we present global biomass distributions of the four phytoplankton and two zooplankton functional types FOSI-HR (panels a–f) and fish types from FEISTY-HR (panels g–i). Also, please refer to Figure S6 for a FOSI-LR version of this figure, which looks similar.

The small phytoplankton (SP) functional type represents a wide variety of algal species, from *Prochlorococcus* and *Synechococcus* in central ocean gyres to cryptophytes or *Phaeocystis* in polar ecosystems. Thus, the SP functional type has very broad spatial coverage in FOSI-HR. Concentrations of SP range from ∼0.4 to 0.6 g C m^{-2} for all oceanic regions outside of areas that are covered by sea ice for part of the year (Figure 8a). In sea ice zones, SP concentrations drop to roughly 0.2 g C m^{-2}, likely due to the strong seasonal light limitation imparted by sea ice and the solar zenith angle cycle. SP

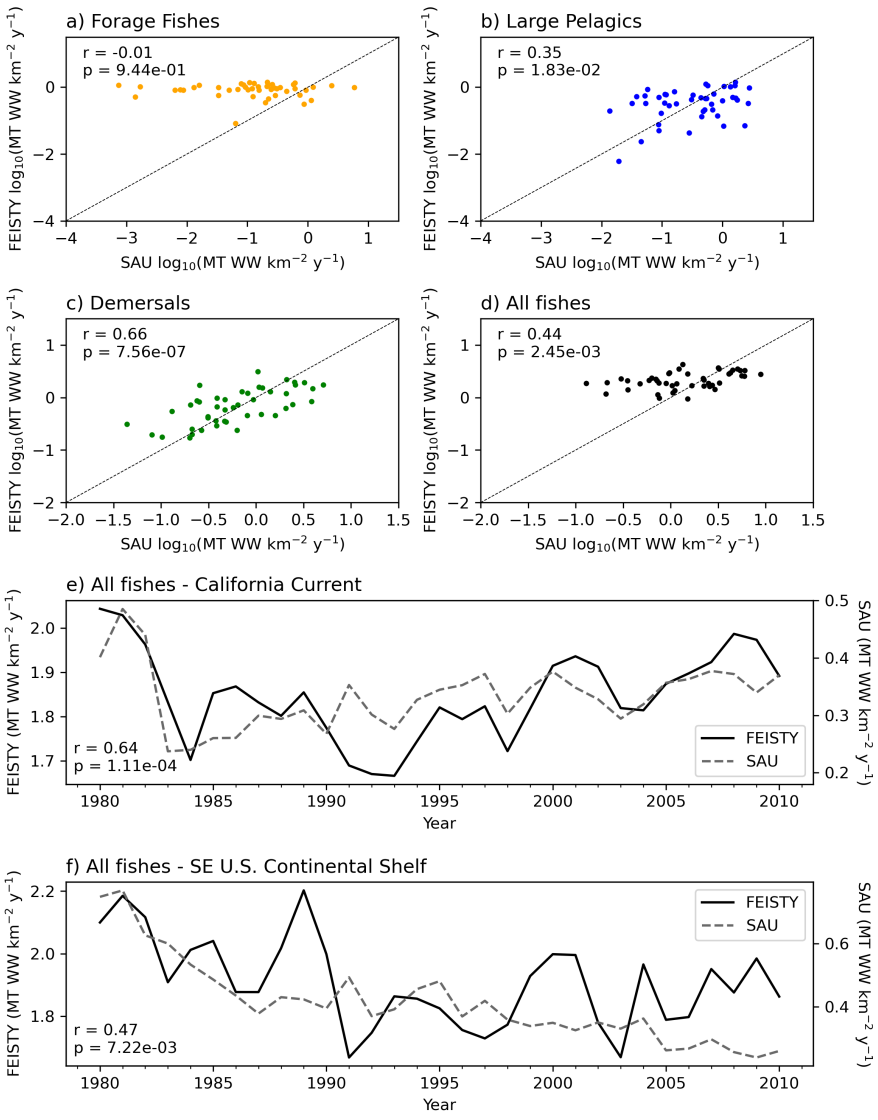

Figure 7: Fish catch yields from FEISTY-HR forced by the FOSI-HR simulation compared to the Sea Around Us (SAU) dataset for 45 Large Marine Ecosystems (LMEs), a subset of the total 66 LMEs where outliers that had low fishing effort and low catch were eliminated. The top four panels (a–d) show scatter plots of SAU versus FEISTY-HR fish catches - each dot represents the "mean" fish catch in an LME. For SAU data, we take the mean of the top 10 fish SAU catches for each LME. For FEISTY data, we take the mean of the catch data over the 1980-2010 period; this time period was chosen because the SAU catch data spans from 1950-2010 while the FEISTY catch data spans from 1980-2021, so 1980-2010 is the overlap between the two datasets. See Methods section 2.3 for further details. Panels e and f show time-series of fish catches from SAU and FEISTY-HR for the California Current and Southeast U.S. Continental Shelf LMEs. Correlation coefficients (r values) of the log10 catches for FEISTY-HR and SAU catches are indicated in panels a –d, while correlations between the SAU and FEISTY-HR timeseries are indicated in panels e and f. Note the different y-axis scales for SAU and FEISTY in panels e and f. See Figure S5 for a FEISTY-LR version of this figure.

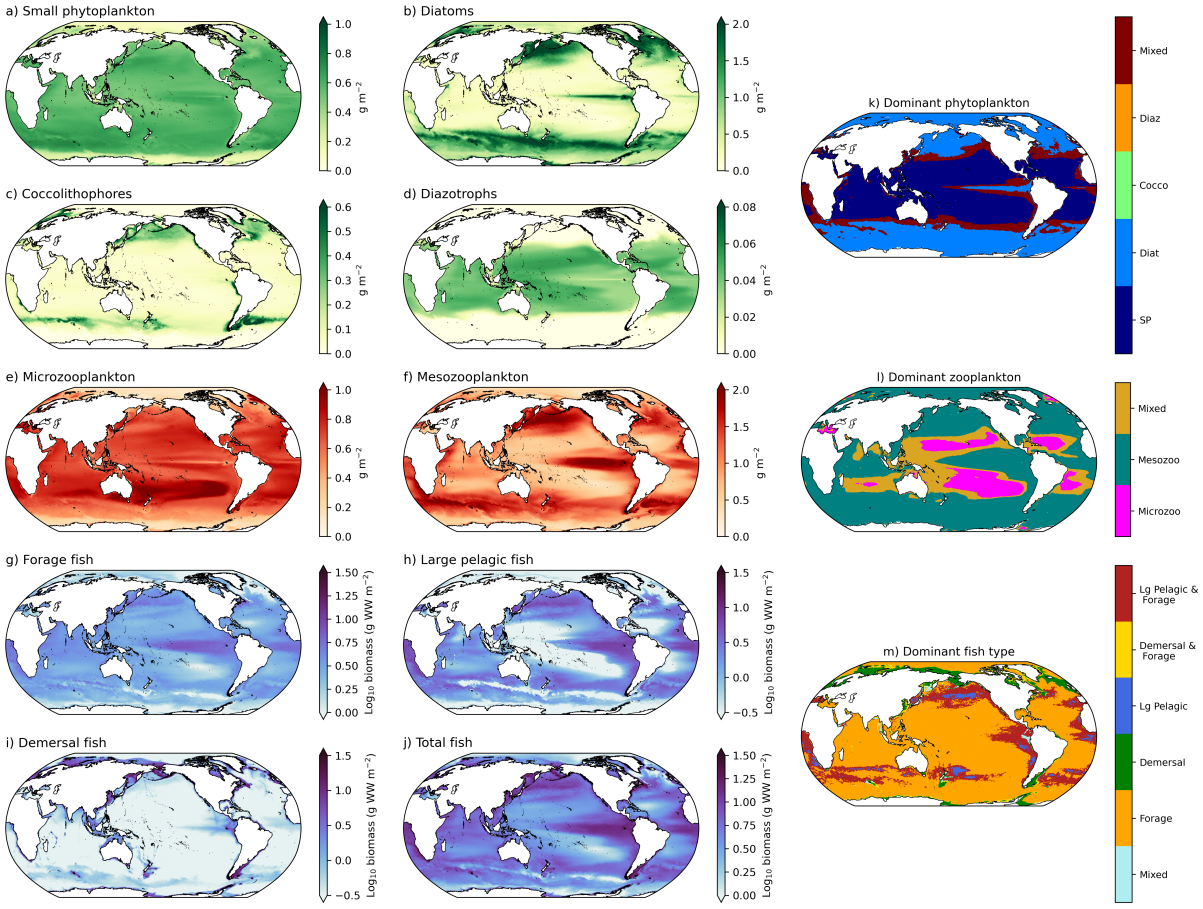

Figure 8: Depth-integrated mean biomass (averaged over years 1980–2005) for phytoplankton (a–d), zooplankton (e–f), and fish (g–j) from FOSI-HR and FEISTY-HR simulations. Note the varying color bar scales for each map. Dominant types for each group are shown along the right side of the figure (panels k–m). For phytoplankton and zooplankton, dominant type was determined as the type that comprised >50% of biomass. For fish, dominant type was determined as follows: areas where a single functional type comprised >50% of all fish biomass were classified as dominated by that type. Areas where no single type comprised >50% of biomass, but two types combined comprised >80%, were classified as co-dominated by two types. Areas where no single type comprised >50% of biomass and two types were not co-dominant were classified as mixed dominance.

fare well under nutrient limitation and thus make up the majority (>50%) of phytoplankton biomass in the nutrient-limited ocean gyres (Figure 8k). In contrast, the diatom functional type thrives in nutrient-rich high latitude environments; the highest concentrations of diatoms are in the subantarctic Southern Ocean, as well as the North Pacific and North Atlantic (Figure 8b). Diatoms are favored in light-limited environments due to their greater potential to increase their chlorophyll to carbon ratio than SP (Table 1). Indeed they are the dominant phytoplankton type in regions polewards of ∼45° latitude (Figure 8k). Like SP, diatoms are also in low abundance in the Arctic and Antarctic sea ice zones, compared to other regions of the ocean, despite being the dominant functional type in these light-limited regions.

While coccolithophore and diazotroph PFTs account for smaller portions of phytoplankton biomass than SP or diatoms, they have important functional roles in global biogeochemistry. Coccolithophores synthesize a calcium carbonate shell around their single cell and thus are a critical component of the carbon cycle, influencing air-sea CO_2 exchange, as well as ballasting organic matter to the deep sea (Krumhardt et al., 2020). Diazotrophs, on the other hand, can fix dissolved N_2 gas, and thus are not limited in their production by nitrogen availability; diazotrophs comprise a critical part of the nitrogen cycle and are an important source of "new" nitrogen into the upper ocean (Dugdale & Goering, 1967). The parameterization of coccolithophores in CESM is largely based on *E. huxleyi* (Krumhardt et al., 2017), the most well-studied coccolithophore. As such, the coccolithophore distribution (Figure 8c) follows that of *E. huxleyi* (see Balch et al., 2005), with blooms in temperate oceanic environments with plentiful iron availability, such as the Patagonian shelf, the North Atlantic and the North Pacific. Coccolithophore biomass is generally <0.1 g m^{-2} in low latitude regions and polar waters, where nutrient availability and temperature limits their production, respectively. Diazotrophs also have a strong thermal component to their biogeography, as they are confined to water temperatures >15°C in MARBL (Long et al., 2021). The geographic distribution of the diazotroph functional type shows that they are mainly in warm, nitrogen-limited regions, matching well with maps produced using an inverse modeling approach (Wang et al., 2019). Coccolithophores and diazotrophs do not dominate the phytoplankton communities anywhere in the global ocean in an annual mean sense (Figure 8k), though coccolithophores do show some summertime blooms that may lead them to be the dominant phytoplankton type on a seasonal basis in some regions (not shown).

Zooplankton distributions largely follow the source of their primary phytoplankton food source (Figure 8e and f). Microzooplankton mainly rely on SP for grazing and thus they show a broad global distribution, as with SP. Microzooplankton are only the dominant zooplankton in the central ocean gyres, with particularly high biomass in the South Pacific (Figure 8e,l). Mesozooplankton, in constrast, mainly graze on diatoms (Table 3) and thus their geographic distribution pattern mainly follows that of diatoms. Mesozooplankton can also be part of a longer food chain, however, from SP to microzooplankton to mesozooplankton, for example (Figure 1, left side). Therefore mesozooplankton dominate 76% of the ocean on average in the FOSI-HR, outside of the central gyres (Figure 8f and l). Mesozooplankton act as a food resource for forage and large pelagic fish in FEISTY (Figure 1).

Mean fish distributions of each fish functional type are shown in Figure 8g–i, with total fish biomass shown in Figure 8j. Forage fish show a cosmopolitan distribution, with particularly high biomass in equatorial regions, the North Pacific and the northwest Atlantic. Forage fish tend to dominate the fish biomass in most open ocean regions (see orange areas on Figure 8m). Large pelagic fish biomass has more spatial variability, with high biomass in the same regions mentioned above for forage fish, but with particularly low biomass in the western low latitude Pacific and Atlantic Ocean basins. While large pelagic fish do not dominate much of the ocean in terms of biomass, they do co-dominate with forage fish in some subpolar regions and in the equatorial Pacific. However, there is also a strip of very low large pelagic fish biomass in the Indian and Pacific sectors of the subantarctic Southern Ocean. Demersal fish are concentrated on the continental shelves (where they are the dominant fish type; green regions in Figure 8m) with low biomass in open ocean regions, as we would expect for this fish type that relies mainly on benthic organisms for nourishment. Demersal fish biomass is also slightly elevated on the ocean ridges in the Southern Ocean. In general, these large-scale fish biomass distributions are remarkably similar to those shown in Petrik et al. (2019), despite being forced by a different ESM at a lower resolution.

To summarize, large scale biogeography features described above are consistent between FOSI-HR and FOSI-LR (Table 4 and Figure S6). However, taking a closer look at regional trophodynamics allows us to examine the unique features of the FOSI-HR simulation.

4.2 High resolution regional scale trophodynamics

Resolving mesoscale dynamics is important for capturing influential physical features in various ocean regions, especially coastal areas. Resolving details of topography and ocean physics to 0.1° (∼10 km horizontal resolution) allows for a more accurate representation of coastal currents, upwelling, and other characteristic circulation features relevant for regional scales (Chang et al., 2023). Monthly snapshots from the FOSI-HR show how marine NPP responds to these physical dynamics, compared to the standard 1° version of CESM (Figure 9). We chose shapshots of NPP for months of peak productivity in each region; California Current and Southeast U.S. Shelf NPP peaks in March, while Antarctic productivity peaks in December in FOSI-HR.

Marine phytoplankton have short life cycles and respond to short-term, fine-scale perturbations in their environment. In the California Current LME, upwelling of nutrient-rich waters is more confined to the near shore regions with filaments and eddies moving west. Snapshots from March 1999 of FOSI-HR and FOSI-LR show that NPP responds to this high-nutrient upwelled water (Figure 9a and b); however, the response is much more widespread in the low resolution version when these fine scale dynamics are not resolved. This indicates that broader upwelling in FOSI-LR results in a saturation of phytoplankton growth over a larger area, whereas in FOSI-HR, high productivity is confined to a more narrow strip of coastal upwelling. Generally, NPP in the California Current is higher in FOSI-LR than FOSI-HR throughout the simulations, but the area-averaged interannual variability is similar in both simulations (Figure 9c). While we do not delve into more rigorous analysis here, we speculate that several mesoscale-related processes could be contributing to lower overall productivity in the high-resolution simulation. First, resolving mesoscale features may act to reduce biological production via eddy-induced lateral transport and subduction of nutrients (Gruber et al., 2011). Secondly, as nutrients are likely more concentrated in mesoscale features and along the coast in FOSI-HR than in FOSI-LR, this may act to shift the phytoplankton composition to more diatoms (as opposed to small phytoplankton), thus increasing export of carbon and nutrients and leading to less recycled NPP in the 0.1° simulation. Lastly, nutrient availability may not be the dominant driving factor this early in the growing season; factors affecting light availability, such as mixed layer depth, could also impact phytoplankton growth especially during the springtime (March snapshots are shown in Figure 9a–f). See section 4.4 for further discussion on fine scale modulation of the ocean environment.

Maps of the southeast U.S. shelf LME also show the importance of resolving fine scale coastal processes (Figure 9d–f). Resolving the Gulf Stream and the fine scale topography in the Caribbean basin lead to completely different spatial distributions of NPP around the southeast U.S. coast. For instance, the loop current (and spawning eddies) appear in FOSI-HR (Figure 9d) but are absent in FOSI-LR (Figure 9e). Similarly, a well resolved Gulf Stream results in depressed NPP right along the eastern coast of the U.S. and elevated NPP just off the shelf; these features are not resolved in FOSI-LR (Figure 9e). Thus the FOSI-HR simulation has roughly 20% more productivity than FOSI-LR with somewhat different phasing of interannual variability. Higher NPP in the FOSI-HR than the FOSI-LR in this region is likely due to mesoscale modulation of bottom up factors that work to augment phytoplankton growth in FOSI-HR (see section 4.4 for more discussion on this topic).

Antarctic productivity also shows some small scale differences between the FOSI-HR and FOSI-LR. NPP during December of 1998 (Figure 9g and h) is higher along the coastal regions, including the Ross Sea, in FOSI-HR, as compared to FOSI-LR. This likely concerns sea ice dynamics; specifically coastal polynyas are opening up earlier in the season in the high-resolution simulation. Further, NPP is more concentrated in FOSI-HR around ∼60°S (on the outer edges of Figure 9g and h), likely from eddy-induced mixing in the Antarctic circumpolar current. The time-series shown in Figure 9i is for the Ross Sea region (see boxed region on map). While the simulations match well in overall NPP magnitude, the magnitude of variability in FOSI-HR is greater (standard deviation is 1.88 mmol m^{-2} d^{-1} for the FOSI-HR and 1.37 for the FOSI-LR; Figure 9f). Furthermore, it appears that the Ross Sea polynya has opened up earlier in the season in FOSI-HR, as NPP is greater (darker green on the maps). Further work is needed to understand how model resolution affects the sea ice retreat-advance and how this may affect Antarctic productivity and potentially food resources for higher trophic levels.

Additional snapshots of the marine ecosystem in FOSI-HR show that important components of the marine ecosystem respond to mesoscale variability in ocean physics. As an example, we show snapshots from August 1995 of mesozooplankton production, POC flux, and fish production in the Northwest Pacific Kuroshio current region (Figures 10 and S7). To put this snapshot in context, SST, NPP, and fish biomass were all in the middle of the range for the FOSI-HR and FEISTY-HR

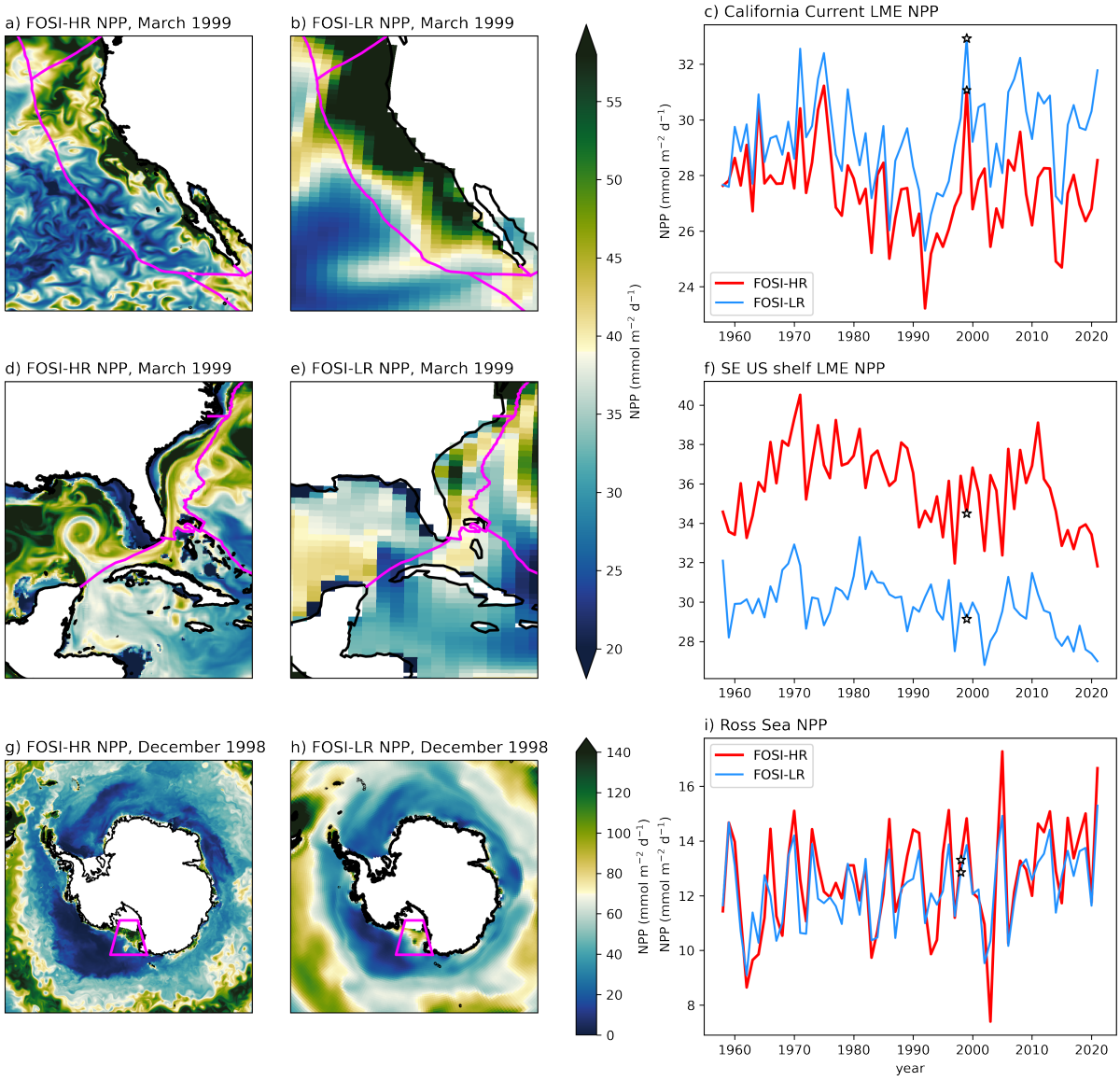

Figure 9: The influence of resolution on simulating NPP in coastal ecosystems: California Current (panels a – c), southeast U.S. (panels d – f), and Antarctic coastal region, Ross Sea timeseries (panels g – i). The top two rows use Large Marine Ecosystem (LME) masks for the California Current and Southeast U.S. Shelf to create time-series (outlines for LMEs shown on maps), while the bottom row timeseries is for the Ross Sea region (see box on maps g and h; the latitude and longitude boundaries for this region are 80°S to 70°S and 165°E to 195°E).

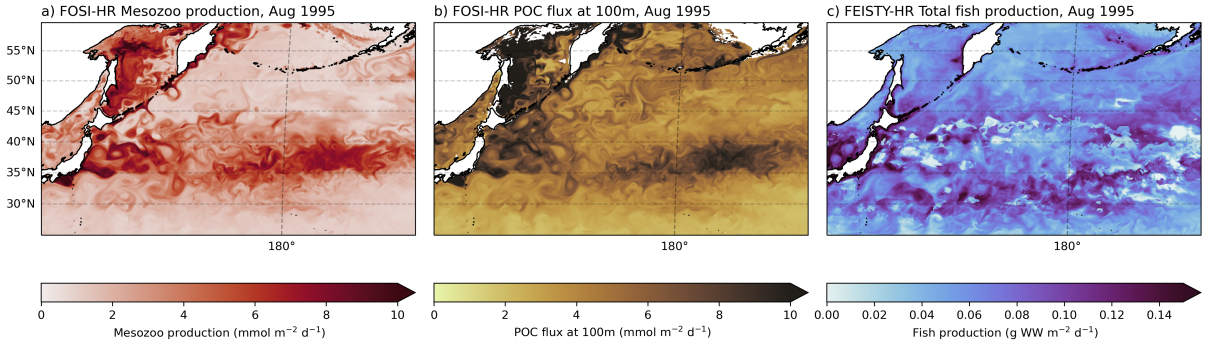

Figure 10: Kuroshio Current region mesozooplankton production and particulate organic carbon (POC) flux for August 1995 of FOSI-HR, and total fish biomass from August 1995 of FEISTY-HR.

time-series for this region (Figure S1b–c). Mesozooplankton production in August of 1995 is elevated in energetic Kuroshio current eddies propagating eastward over the dateline. This is likely due to mixing and eastward transport of high nutrient water from depth, which fuels phytoplankton growth and subsequent mesozooplankton grazing and production. POC flux is also elevated and shows the imprint of mesoscale features. Since POC flux in CESM is simulated implicitly following Armstrong et al. (2001), i.e., sinking POC is distributed instantaneously across the water column, it retains the mesoscale imprints from the upper ocean. We also show total fish production from FEISTY-HR in Figure 10c for the same month and year as the upper two panels. While fish production appears to have imprints from mesoscale variability, it does not follow the same regional patterns as mesozooplankton biomass and POC flux. Rather, fish production in August 1995 is quite low in the 35°N to 40°N band where mesozooplankton and POC flux are elevated, and higher to the north and south of that band. Including fish movement in FEISTY could potentially lead to smoother fish biomass and production at monthly timescales. Interestingly, the 1° CESM version of this figure shows a different spatial distribution of fish production during August 1995 (Figure S7). This leads to questions about the controls on spatial and temporal variability in fish production and biomass on regional scales.

The FOSI-HR and FEISTY-HR simulations can also be used to examine the impacts of extreme climate events on the marine food chain. As an example for the North Pacific region, we created maps from May 2015 of FOSI-HR and FEISTY-HR to illustrate how a marine heatwave may influence the ocean ecosystem (Figure 11). During 2014-2015, the Northeast Pacific experienced a strong marine heatwave (Di Lorenzo & Mantua, 2016), commonly referred to as "the blob."; see Figure S1e for a time-series of SST in this region. While some of the biogeochemical imprints of this marine heatwave have been explored (Mogen et al., 2022), analysis of the impacts on nutrients to fish at 0.1° could also offer insights into this extreme event. In Figure 11 we show anomalies of sea surface temperature (SST), NPP, mesozooplankton biomass, and fish biomass during May of 2015. In general the subpolar part of the North Pacific shows increases in NPP and mesozooplankton in response to the warm SSTs, while the southern part of the domain showed decreases in these fields. This finding is generally in agreement with the observed chlorophyll response to marine heatwaves in the North Pacific (Noh et al., 2022). Fish biomass in FEISTY-HR shows anomalous declines along ~40°N, with slight increases to the north and south. Notably fish biomass anomalies look different in FEISTY-LR, with decreases in northern and eastern regions of the North Pacific, and increases to the south (Figure S8).

The California Current region also shows some interesting anomalies in response to the heatwave. NPP along the North American coast increases to the north and decreases to the south in FOSI-HR, though mesozooplankton biomass does not mirror these changes as it does in open ocean regions. Instead, mesozooplankton increases are constrained to the coastal region between Mendocino and Point Conception. Fish biomass is also slightly elevated in this small area in FEISTY-HR, but shows decreases along the southern part of the California coast.

Indeed, fish biomass fields from FEISTY forced by the FOSI-HR also show interesting interannual variability. In order to illustrate this variability, we show annual mean time-series plots from different oceanic regimes with maps of dominant fish type for several years in Figure 12 (see also Figure S9 for a FOSI-LR version of this figure). We chose these regions because they were diverse in terms of dominant fish type, they showed interesting interannual variability, and they span a range of oceanic

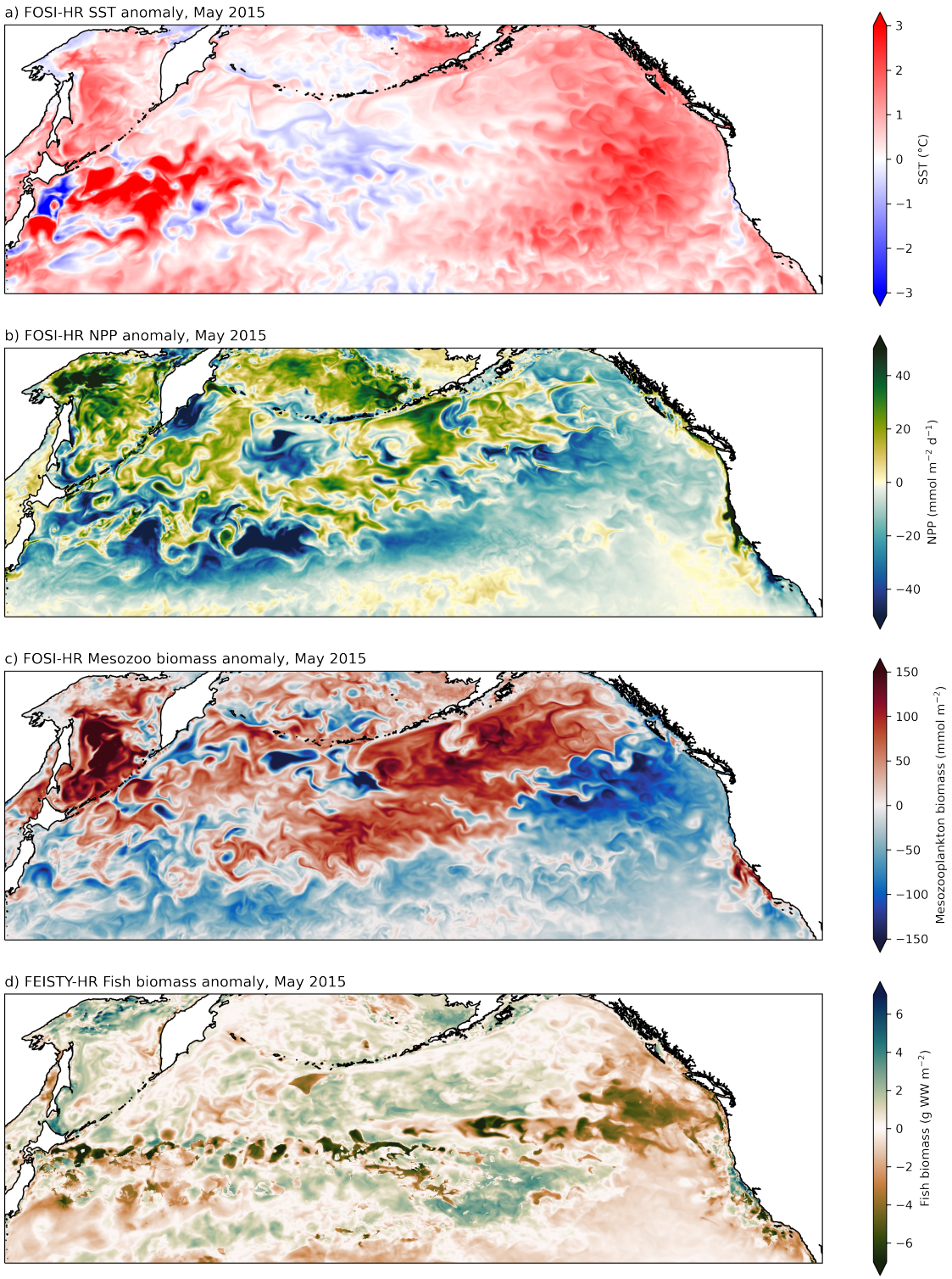

Figure 11: Biogeochemical and ecosystem effects from the 2014/2015 marine heatwave in the North Pacific in the FOSI-HR. These maps show anomalies in sea surface temperature (SST; panel a), net primary productivity (NPP; panel b), mesozooplankton biomass (panel c), and total fish biomass (panel d) during May of 2015 relative to a baseline May average (mean over Mays, 1980-2000) in FOSI-HR and FEISTY-HR. See Figure S8 for a FOSI-LR/FEISTY-LR version of this figure.

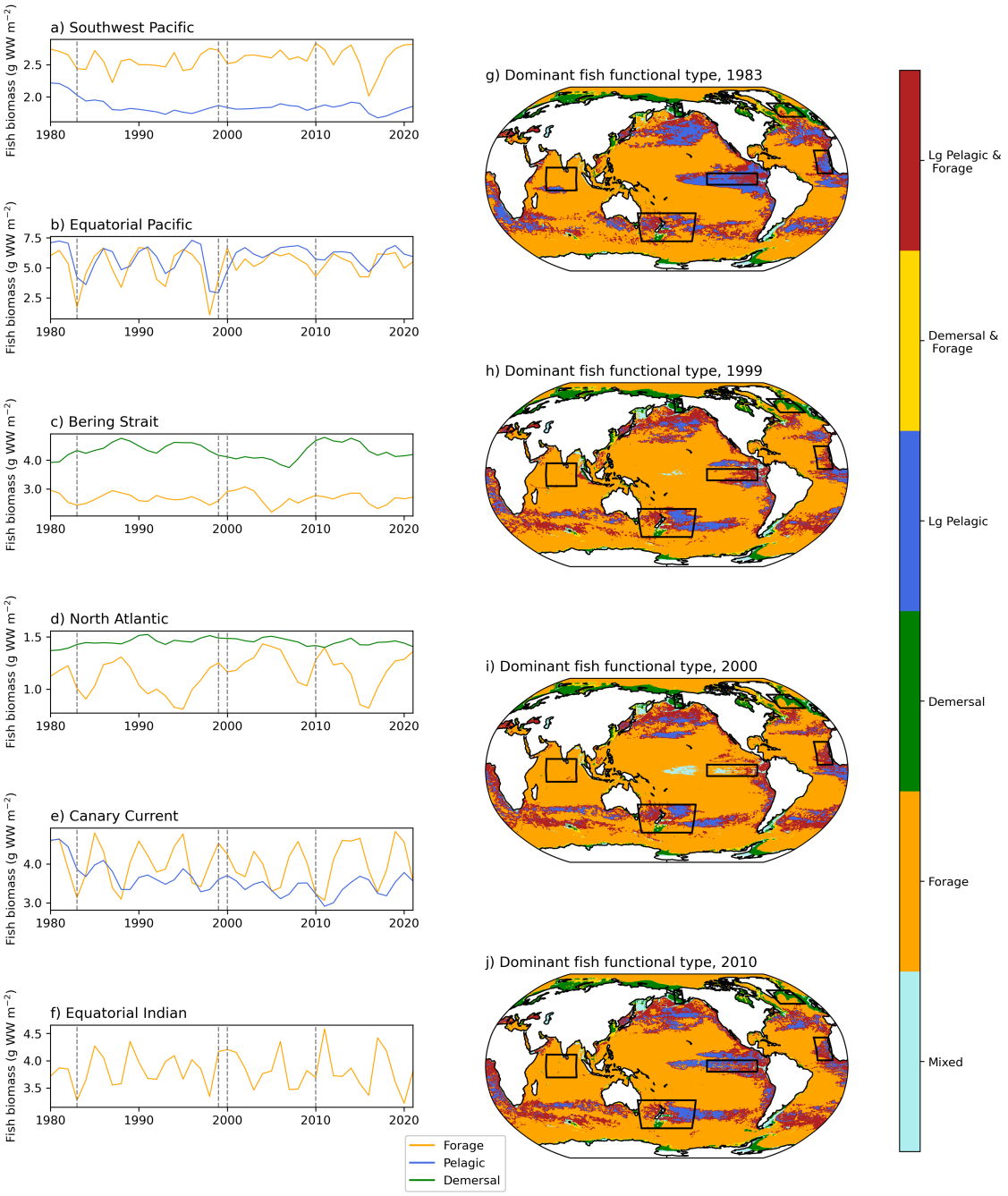

Figure 12: Interannual variability in fish biomass in various oceanic regions from the FEISTY-HR simulation. Timeseries for 6 diverse oceanic regions and maps showing how dominant fish types and overall fish biomass may vary from year to year. The dashed lines on panels a – f indicate the timing of snapshots shown in panels g – j. See Figure 8 caption for details about dominant fish type classification. See Figure S9 for a FEISTY-LR version of this figure. Latitude and longitude boundaries for these six regions are as follows: Southwest Pacific (panel a; 55°S to 30°S and 150°E to 210°E), Equatorial Pacific (panel b; 5°S to 5°N and 140°W to 90°W), Bering Strait (panel c; 55°N to 68°N and 170°W to 160°W), North Atlantic (panel d; 55°N to 68°N and 45°W to 15°W), Canary Current (panel e; 5°N to 25°N and 30°W to 15°W), and Equatorial Indian (panel f; 10°S to 10°N and 60°E to 90°E).

environments from the tropics to the high latitudes; exact latitude/longitude boundaries are specified in the Figure 12 caption. Climate forcing can cause variations in fish biomass, as the dominant fish type in a geographical location may vary over the course of the 1980 to 2021 FEISTY-HR simulation, hence the variable dominant fish type maps shown in Figure 12g–j. While we have not investigated long term trends in fish biomass associated with, e.g., oceanic warming, we note that large pelagic fish in the southwest Pacific and Canary Current appear to decrease over time (Figure 12a and e).

One particularly interesting region is the equatorial Pacific, which is dominated by both forage and large pelagic fish types (Figure 12b). During the 1982-1983, 1997-1998, and 2014-2016 El Niños, both forage and large pelagic fish drop in biomass. The year after an El Niño event, forage fish rebound faster and become dominant over the large pelagic fish. Large pelagic fish, however, recover ∼2 years after an El Niño event. Note that in the FEISTY model, fish cannot move laterally between grid cells, meaning that they cannot avoid unfavorable climatic conditions. This is in contrast to real life, where fish populations can migrate in response to, for example, the elevated temperatures caused by El Niño (e.g. Lehodey et al., 2006). This may make the ecosystem response observed in FEISTY-HR less realistic, especially at high-resolution where lack of modeling fish movement may be a bigger issue than when the grid cells in the model are bigger, as in FOSI-LR.

In general, forage fish show more interannual variability than the other FEISTY fish types in the regions we examine. For example, in the North Atlantic, demersal fish (e.g., North Atlantic cod) are the dominant type, but forage fish show much larger fluctuations than demersal fish. Forage fish could show heightened sensitivity to climate variations given their smaller size and shorter time to reach maturity.

4.3 Ocean acidification over the past 64 years

One important feature of FOSI-HR is the implementation of historical atmospheric CO_2 forcing, thereby creating a reconstruction of ocean acidification from anthropogenic carbon emissions over the period 1958 to 2021. A complication of analyzing the anthropogenic increase is CO_2 drift in the natural carbon system. It is not feasible to spin up the FOSI-HR configuration due to computational costs. We mitigate this in our analysis by using two parallel carbonate systems: one where the ocean is exposed to anthropogenic atmospheric CO_2 concentrations and one with preindustrial (285 μatm) CO_2 concentrations. Anthropogenic CO_2 can be computed by differencing these two systems, accounting for drift in the natural carbon system. Applying this differencing to the pH field, we determined that global mean pH of the ocean in 2021 was lower by 0.089 since the preindustrial era due to the absorption of anthropogenic carbon into the ocean in FOSI-HR.

The coccolithophore phytoplankton functional type in the MARBL ecosystem configuration is sensitive in its growth and calcification to environmental conditions, including ocean acidification (Krumhardt et al., 2020; Krumhardt et al., 2019). We focus our attention on the North Atlantic to assess the effects of environmental changes on coccolithophores over the past 64 years (Figures 13 and S10). Here, coccolithophores form regional blooms in the summertime that show in the imprints of mesoscale ocean dynamics (see Figure 13a for a snapshot from July 2005 (a particularly warm year in the North Atlantic; see Figure S1h), when coccolithophores blooms are underway). This region has accumulated ∼70 mmol m^{-3} anthropogenic dissolved inorganic carbon (DIC) in the surface ocean (upper 10 m) since industrialization, dropping pH by roughly 0.1 units (Figure 13b and c). Though pH has dropped across the entire North Atlantic domain shown in Figure 13 the eastern part shows less of of a drop, while the coastal region along North America has the steepest declines in pH. SST has also warmed over most of the North Atlantic in FOSI-HR, except for an area of cooling just south of Greenland and some small patches along the Gulf Stream.

These environmental changes have resulted in changes to the coccolithophore calcification. The particulate inorganic carbon to particulate organic carbon ratio (PIC/POC) of coccolithophores is an indication of how calcified they are. Changes in aqueous CO_2 concentration ($CO_{2(aq)}$), nutrient limitation, and temperature can all affect coccolithophore PIC/POC (Krumhardt et al., 2019; Krumhardt et al., 2017).The negative effect of ocean acidification (i.e., increasing $CO_{2(aq)}$) on PIC/POC is most prominent, as large areas of the North Atlantic show decreases in coccolithophore PIC/POC ratios over the past 64 years in this CESM simulation (Figure 13e). However, increasing temperature would have the opposite effect: warmer temperatures cause higher PIC/POC. Indeed, the subtropical parts of the North Atlantic in the southern part of the domain shown in Figure 13 show slightly increased PIC/POC ratios (for more details on the coccolithophore parameterization see Krumhardt et al.,

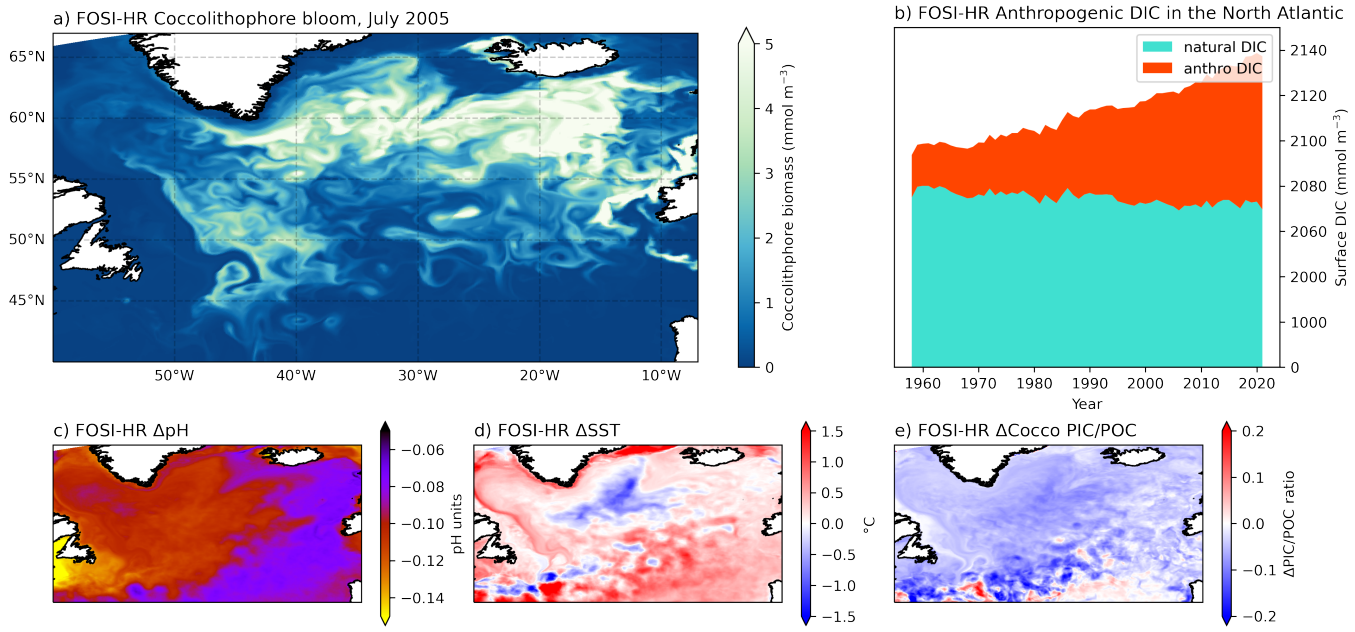

Figure 13: Ocean acidification and warming influences North Atlantic coccolithophores. Panel a shows an example of a modeled coccolithophore bloom in the North Atlantic region during July, 2005 of the FOSI-HR simulation. Panel b shows a time series of surface (top 10 m) dissolved inorganic carbon (DIC) concentration in this region (60°W to 7.6°E, 38.8°N to 67.6°N) over the course of the simulation; note that the y-axis ticks on panel b are not evenly spaced. Panels c, d and e show changes over the period 1958 to 2021 (last 5 years-mean minus first 5 years-mean) in pH, sea surface temperature (SST), and the coccolithophore particulate inorganic carbon to particulate organic carbon (PIC/POC) ratio, respectively. See Figure S10 for a FOSI-LR version of this figure.

2020; Krumhardt et al., 2019; Krumhardt et al., 2017). Furthermore, increasing nutrient limitation also causes increased PIC/POC (van Bleijswijk et al., 1994). Ocean stratification and subsequent increases in nutrient limitation could also work to increase PIC/POC. Thus, increased PIC/POC in the southern part of the domain shown in Figure 13 could also stem from warming-induced ocean stratification and decreased nutrient availability. The changes in coccolithophore PIC/POC shown in Figure 13e are a combination of several environmental changes in the North Atlantic occurring over the recent past.

4.4 Fine scale environmental modulation of the marine ecosystem

Mesoscale features modulate light, nutrients, and temperature, and thereby have the capacity to affect ecosystem dynamics. Resolving ocean processes on the scales of 10 km improves the mean state representation in areas of vigorous mesoscale activity, such as coastal and upwelling regions, and it also allows for resolving the larger baroclinic eddies in most regions of the ocean (Chang et al., 2020; Kirtman et al., 2012).

As well as being a strong upwelling area, the equatorial Pacific is also an area of strong eddy activity in the form of tropical instability waves (TIWs), westward propagating features with wave lengths on the order of 1000 km and periods of 13-40 days (Halpern et al., 1988; Legeckis, 1977; Miller et al., 1985; Qiao & Weisberg, 1995). The passage of a TIW not only modifies temperature gradients and currents, but also biogeochemistry. Eddebbar et al. (2021) demonstrate that TIWs modify the availability of dissolved oxygen using the same ocean model as used in FOSI-HR. Eddebbar et al. (2021) also demonstrate that the equatorial undercurrent and the oxygen minimum zone are better represented in FOSI-HR than in FOSI-LR (see also Section 3.2). While there is some indication of TIW activity in FOSI-LR, the fronts are much more distinct in the FOSI-HR (Fig. 14). The 5-day average SST shows well-defined wave structures emanating from the eastern tropical Pacific and extending from the equator into the Northern Hemisphere. A longitudinal transect along 2°N shows the clearly-defined frontal features in SST and their relationship with NPP: strong temperature gradients coincide with strong NPP peaks on the cold sides of the fronts, likely due to increased nutrient availability in colder (upwelled) waters. This relationship is more pronounced in FOSI-HR than in FOSI-LR, allowing for detailed investigation of the impact of these mesoscale features in an already highly productive area of the ocean.

Indeed mesoscale dynamics influence bottom-up factors affecting phytoplankton growth: light, nutrients, and temperature. Figure 15 depicts several longitudinal transects of nutrients and temperature for three regions, showing how mesoscale features may modify the upper ocean environment. Figure 15a,b shows a transect along 2°N in the equatorial Pacific (same area/time as in Figure 14, except this figure is made using monthly means) from the FOSI-HR (see Figure S11 for a FOSI-LR version of the figure). The increased horizontal resolution in FOSI-HR allows small variations in iron concentrations, the most limiting nutrient for phytoplankton growth in this region, and temperature, across the water column in the equatorial Pacific. Mixed layer depth, which affects both light and nutrient availability, is also influenced by mesoscale activity showing much more small variations, as compared to the FOSI-LR (Figure S11a,b), along this transect in the equatorial Pacific. The California Current and southeast U.S. shelf also have more spatial heterogeneity in nutrients, temperature, and mixed layer depth, as a function of longitude and depth (Figure 15c–f). This variability projects onto phytoplankton growth and influences ocean ecosystems from the bottom up. In contrast, this environmental variability is not present in the FOSI-LR, which shows a much smoother gradation of environmental factors affecting phytoplankton growth over these transects (Figure S11).

Fish distributions also respond to features only resolved by FOSI-HR, in contrast to FOSI-LR. An example of this is the Antarctic coastal current (e.g., see Schubert et al., 2021) in the Amundsen Sea and Bellinghausen Sea region in Western Antarctica (Figure 16) Here, coastal polynyas in the sea ice zone open up in the springtime allowing early light access to the water column and fueling primary production. This coastal springtime bloom is captured by FOSI-HR, but not by FOSI-LR (Figure 16a,b). While some of the NPP is recycled or passed up the pelagic food web, much of the organic carbon produced by the bloom is exported to the seafloor in this shallow coastal shelf. This supplies benthic invertebrates in FEISTY with a food source, which, in turn, are consumed by demersal fish. An example of a demersal fish in this geographic location would be the Antarctic toothfish, an important species to fisheries (Hanchet et al., 2015). Having fine scale features, such as the Antarctic coastal current, resolved could allow more accurate representation of trophodynamics

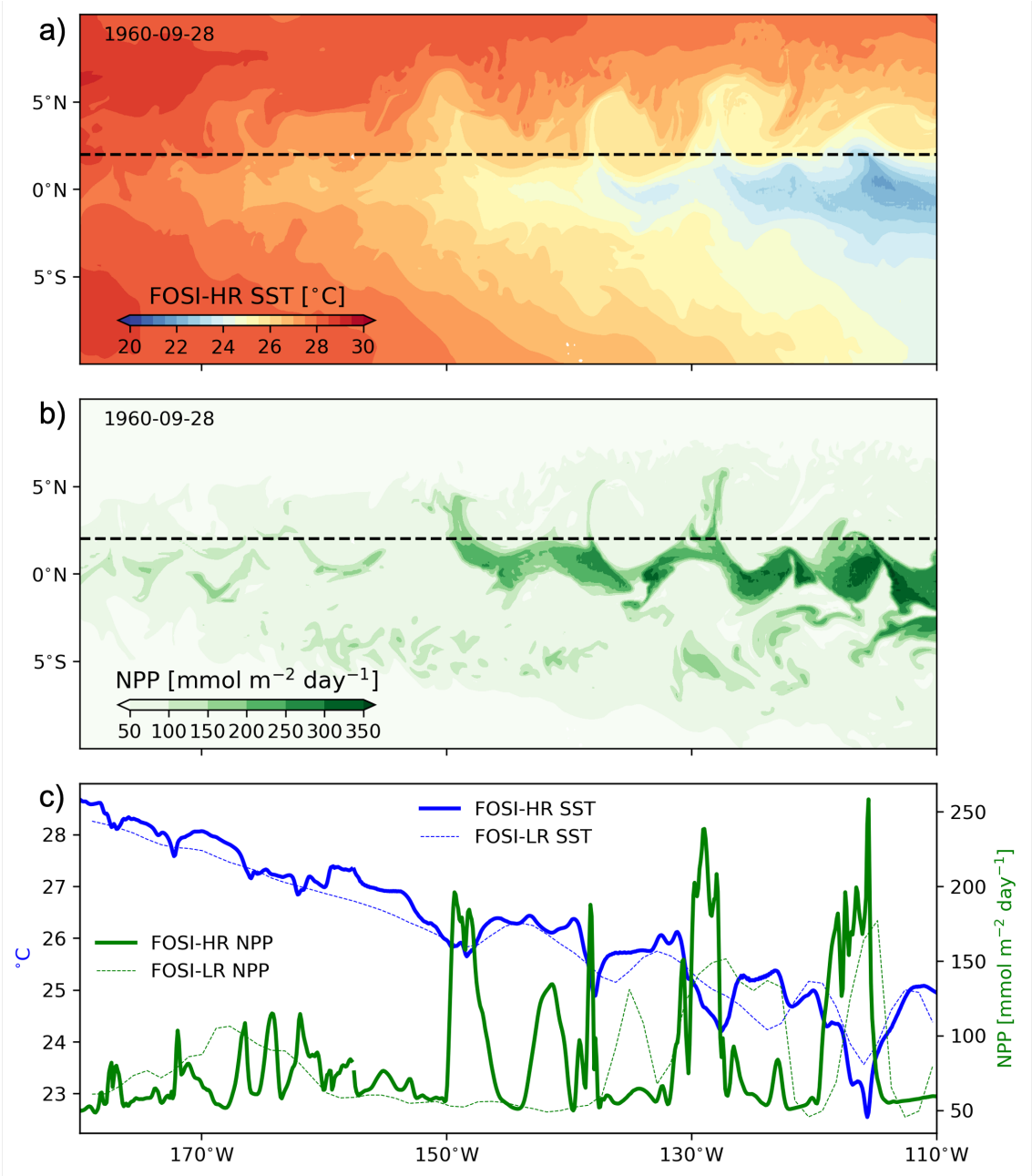

Figure 14: Spatial variability in sea surface temperature (SST) in the equatorial Pacific and its influence on NPP. Snapshots of SST and NPP on September 28, 1960 from the FOSI-HR are shown in panels a and b, respectively. SST and NPP along 2°N transect (shown by black dashed lines in panel a and b) are plotted in panel c with FOSI-HR data in bolder solid lines and FOSI-LR data in thin dashed lines.

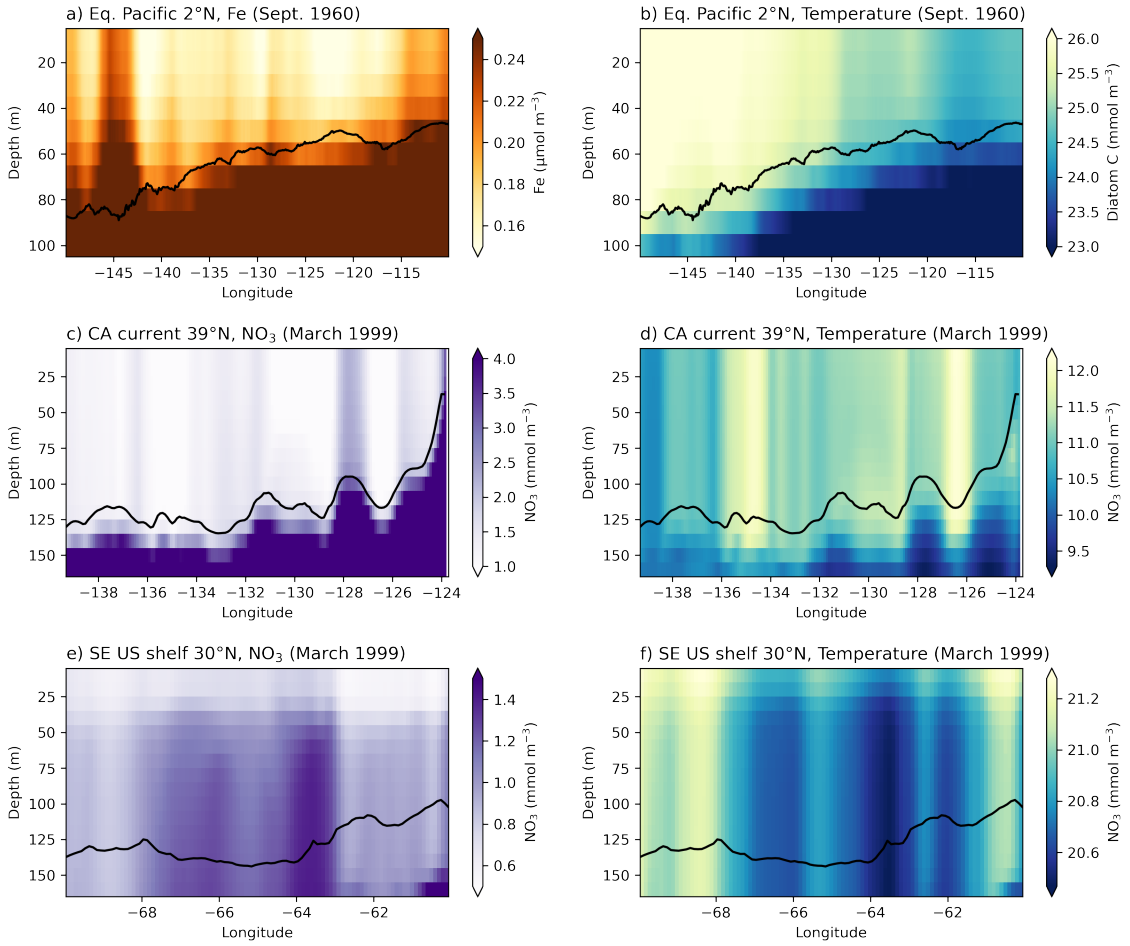

Figure 15: Mesoscale modification of factors affecting phytoplankton growth for the FOSI-HR: nutrients, temperature, and mixed layer depth (indicated by black contour) as a function of longitude and depth. A transect along the equatorial Pacific is shown in the top, a transect through the California Current is shown in the middle row, and a transect along the southeast U.S. shelf is shown on the bottom row. The regions and timeslices shown correspond to those shown in Figure 14 and Figure 9a,b. The left column shows nutrients: Iron (Fe) for panel a; nitrate (NO_3) for panels c and e. The right column shows temperature for each region. Mixed layer depth is shown in all panels by the black contour. See Figure S11 for a FOSI-LR version of this figure.

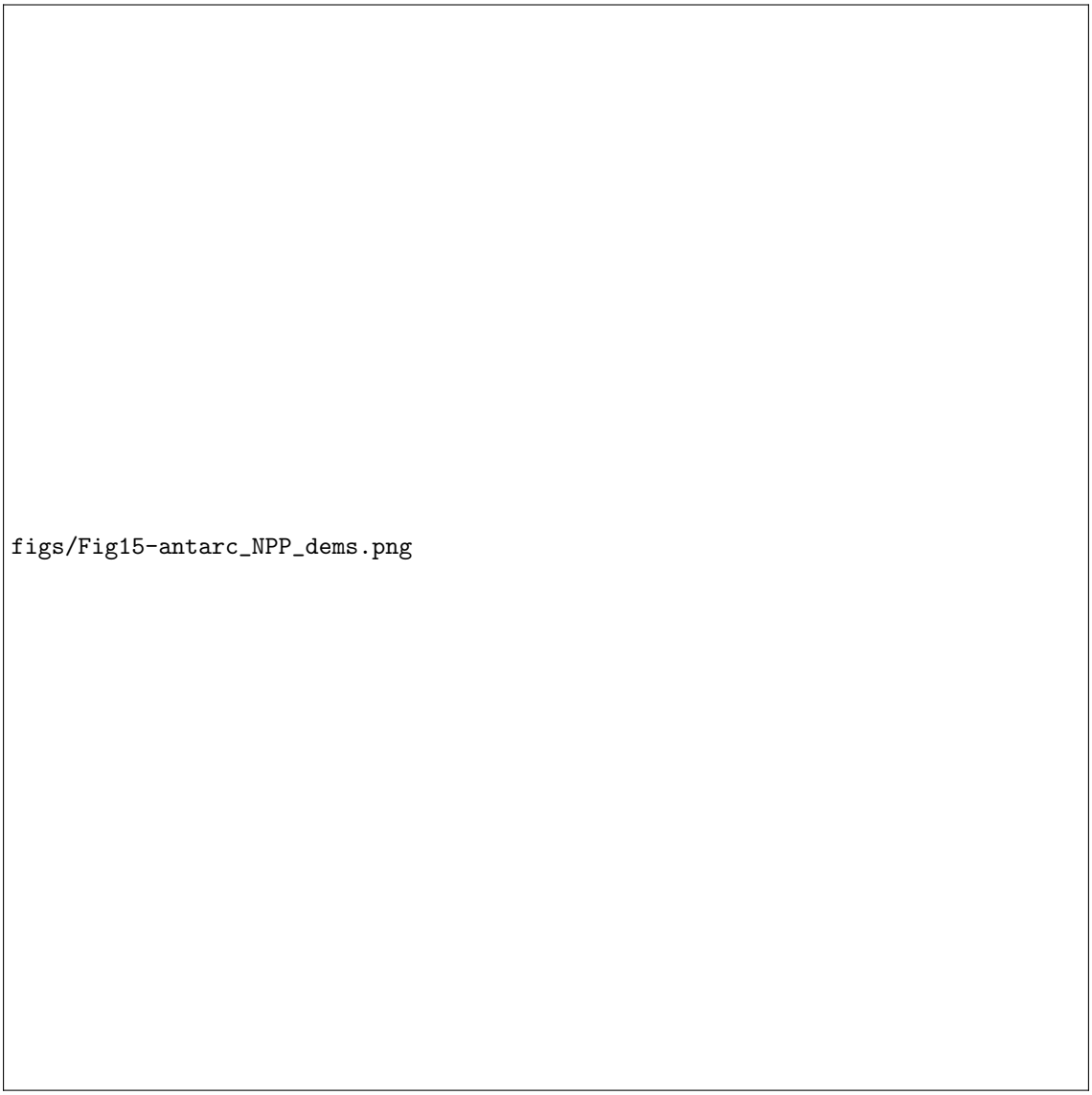

Figure 16: NPP (panels a and b) and Demersal fish biomass (panels c and d) during November 2020 for the Amundsen-Bellinghausen Sea region of the Antarctic coast for FOSI-HR (left) and FOSI-LR (right). Red contours represent 85% sea ice concentration.

that are important for fisheries and understanding food resources for endangered Antarctic marine predators, such as Emperor Penguins (Figure 16 Jenouvrier et al., 2021).

The subantarctic Southern Ocean is a region of vigorous mesoscale eddy activity. The eddies and fronts in this region of the ocean modulate several environmental processes that influence phytoplankton growth (see, e.g., Song et al., 2018), with cascading effects for the rest of the marine ecosystem. In Figure 17, we show snapshots from early December 2020 of various fields from FOSI-HR. Sea surface height (SSH) anomalies are shown by contour lines, demonstrating how eddies may modify trophodynamics. The subantarctic Southern Ocean is characterized by moderately high trophic transfer efficiency, shown here by the z-ratio, the ratio of mesozooplankton production to NPP, an indication of how much energy is transferred up the food web (Figure 17h; Stock et al., 2014a). Eddies modify these mean state dynamics by modulating environmental characteristics that influence phytoplankton growth.

We labeled four eddies in Figure 17: eddies A and B are cyclonic (negative SSH anomalies) and eddies C and D are anticyclonic (positive SSH anomalies). These two types of eddies alter the ocean environment in contrasting ways. Mixed layer depths are deep in the anticyclonic eddies C and D (Figure 17a), resulting in more iron availability (Figure 17b), but also more light limitation for phytoplankton. Indeed productivity of both diatoms and coccolithophores, two important primary producers in this region, is suppressed in anticyclonic eddies C and D, likely due to light limitation. The shallower mixed layer depths in cyclonic eddies A and B result is more light availability but iron becomes more limiting, especially in eddy B. As coccolithophores fare better under iron limitation than diatoms (i.e., they have a lower Fe half saturation constant; Table 1) coccolithophores outcompete diatoms in eddy B (Figure 17d), while diatoms dominate in the eddy A, which has relatively more iron. This demonstrates how eddies can modulate phytoplankton community composition.

Nevertheless, light availability, controlled by the depth of the mixed layer, appears to be the primary factor regulating trophodynamics in this region during this time of the year. Mesozooplankton biomass is especially enriched in eddy A with a shallow mixed layer, while it is starkly suppressed in eddies C and D. These dynamics transfer up the food chain. Forage fish biomass is also suppressed near eddies C and D, but the imprints of these eddies are slightly offset to the northeast, implying a slower response time for forage fish than for phytoplankton and zooplankton. Further, large pelagic fish biomass barely retains the imprints of mesoscale activity, showing a small patch of low biomass near eddy D, with higher biomass towards the eastern side of the box. This is likely to do the longer lifespan and slower response time of these large fish. In short, eddies project environmental variations on to a mean background state and have the capacity to influence how energy/carbon is transformed in the ocean.

5 Conclusions and future directions

In this study we document novel CESM and FEISTY simulations that could be immensely useful for many biogeochemical and oceanographic questions, from studying mesoscale dynamics and their effects on ecosystems to understanding large-scale ocean processes. Applying the FEISTY model to FOSI-HR furthers its applicability for marine food web questions and provides a benchmark for advancing ecological modeling using an Earth System Model. FOSI-HR and FEISTY-HR together effectively provide a reconstruction of the ocean physical state and ecosystem over 64 years. These simulations can be used to investigate recent ocean change and variability, as well as providing initial conditions for high-resolution climate prediction studies.

We evaluate a variety of model fields in FOSI-HR, focusing on metrics relevant for marine ecosystems and biogeochemistry. We show that the FOSI-HR and FEISTY-HR simulations exhibit a reasonable correspondance to available observational datasets and, in many cases, improve upon the lower resolution version of CESM. Sea ice, for example, shows a clear improvement in FOSI-HR, as compared to FOSI-LR, as the FOSI-HR sea ice extents in both hemispheres are closer to those observed (Figure 2). Oxygen and nutrient concentration patterns in the FOSI-HR generally match observations, but there are still some notable biases, showing that some model infidelities cannot be improved with increasing resolution (Figures 3 and 4). Phytoplankton chlorophyll patterns also match available observations in most regions (Figure 5a,b). FOSI-HR NPP correlates well with two observation-based NPP algorithms (Figure 6). Further, while zooplankton observations are sparse, the mesozooplankton observations available correspond well to mesozooplankton biomass in FOSI-HR (Figure 5c,d). Lastly,

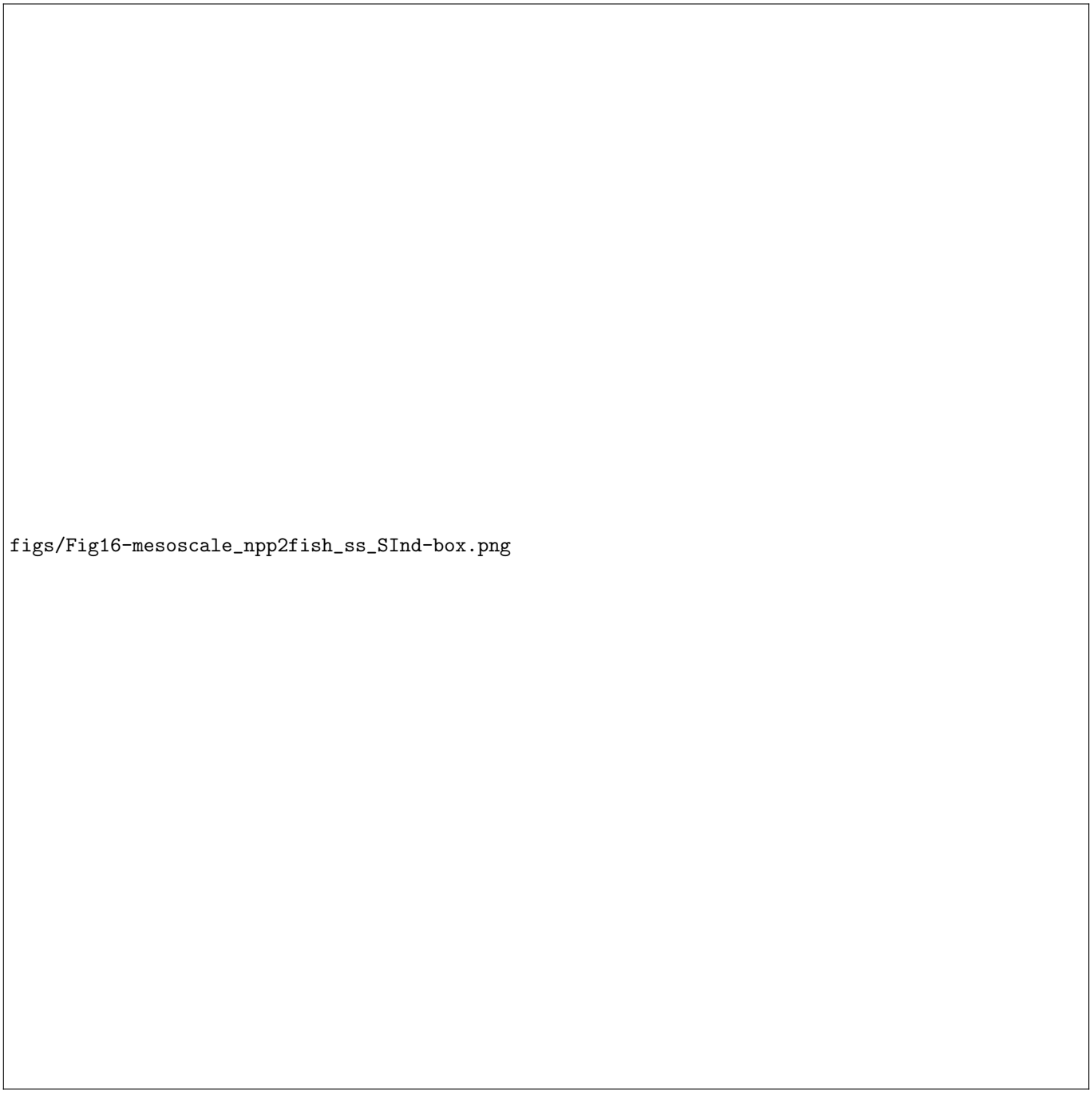

Figure 17: Trophodynamics across scales. Panels a–g show snapshots of daily data for December 1, 2020 for various fields from FOSI-HR, except panel b, which shows the 5-day average for surface iron (Fe) concentration from December 1-5, 2020. Panel h shows the mean z-ratio over the course of the FOSI-HR simulation and the box indicated in the subantarctic Indian section of the Southern Ocean is the region that is shown in panels a–g. Sea surface height (SSH) anomalies are indicated by black contours (except for panel g, they are white) every 3 cm with dashed lines indicating negative SSH anomalies. Four eddies are labeled A–D in order to facilitate discussion of the dynamics in the text. Abbreviations: mixed layer depth (MLD), iron (Fe), net primary productivity (NPP), coccolithophores (cocco), and z-ratio (mesozooplankton production/NPP).

by comparing FEISTY-HR fish catches to historical fish catch records, we show that FEISTY-HR captures mean fish distributions in LMEs reasonably well, as well as capturing interannual variability in fish catches in certain highly-fished regions (Figure 7).

The FOSI-HR and FEISTY-HR simulations offer a consistent framework within which to analyze how upper trophic levels respond to climate forcing. For example, we show that both forage and large pelagic fish drop in biomass in the equatorial Pacific during an El Niño event, but that forage fish populations recover faster (Figure 12). In future studies one could analyze these dynamics, from El Niño impacts on nutrients to plankton to fish, using the FOSI-HR and FEISTY-HR simulations documented here.

Additionally, we show how the eddies captured in FOSI-HR may potentially impact ecosystem dynamics, from better resolved tropical instability waves in the equatorial Pacific (Figure 14) to eddies in the subantarctic Southern Ocean (Figure 17). Indeed, mesoscale activity leaves imprints on physical fields, such as mixed layer depth and temperature. This leads to bottom up forces on the biogeochemistry and ecosystem. Mesozooplankton biomass, for example, still retains a strong imprint of eddies (Figures 10 and 17), but for fish the imprint is more muted.

The FOSI-HR and FEISTY-HR offer a plethora of research opportunities and directions, but there are several limitations to these simulations that could be improved upon in the future. First, it has recently been demonstrated that gelatinous macrozooplankton are a critical component of ocean ecosystems (Clerc et al., 2023; Heneghan et al., 2023; Luo et al., 2022). Gelatinous zooplankton, such as salps and larvaceans, produce fast sinking fecal pellets affecting carbon export (Luo et al., 2022), buffering for example benthic POC flux declines with anthropogenic climate change. Shifts to more gelatinous zooplankton could also negatively affect food quality for fish (Heneghan et al., 2023), an important feedback that is not considered here. Secondly, diel vertical migration (DVM) of zooplankton and fish is not represented in FOSI-HR or FEISTY-HR. Simulation of DVM could affect carbon fluxes, as well as predator prey interactions (Bianchi et al., 2013; Pinti et al., 2021). A DVM representation could further include a light-dependence on visual grazing, potentially affecting the vertical distribution of phytoplankton (Bianchi et al., 2013; Moeller et al., 2019).

Lastly, implementing FEISTY as an online component of CESM-MARBL would enhance its mechanistic realism. Online coupling is straightforward in principle, but requires a decision on whether to treat fish state variables the same as the other prognostic biogeochemical tracers whereby their concentrations are advected and diffused between grid cells, or whether fish can make directed movements in the vertical and horizontal directions. The current absence of horizontal movement implies that fish reside within and explore the entire area of a grid cell, but do not interact with neighboring grid cells. While this assumption may be suitable for forage and demersal fishes in coarse grids like FOSI-LR, it is likely not acceptable for large pelagic fish that make feeding and spawning migrations that span LMEs and ocean basins, nor would it be appropriate for most fish types in higher resolution spatial domains like FOSI-HR. The decisions about behaviorally driven directed swimming, advection, and diffusion would have to be made for each size class of each fish type. Once implemented, the online coupling would allow for examinations of the role of the fish community on nutrient cycling and the biological carbon pump (e.g., Dupont et al., 2023), both directly via waste products and indirectly through top-down effects on mesozooplankton. One of the biggest differences with the online coupling would be partially or fully replacing the non-linear mortality on mesozooplankton in the biogeochemical model with explicit fish predation. Satisfying this energy demand from fishes could provide another constraint on plankton parameterizations.

Here we provide a variety of short analyses in order to showcase the multiple utilities of this simulation data set. While there is still more work to do to advance global marine ecosystem modeling, as noted above, the CESM-FEISTY framework documented here provides an important benchmark. We hope that this high-resolution simulation of the ocean and marine ecosystem, including fish, will be a useful community resource in the coming years.

6 Data and code availability

The full datasets from FOSI-HR, FOSI-LR, FEISTY-HR and FEISTY-LR simulations will be made available on a Globus Guest Collection upon publication of this manuscript. Model data and scripts for making the figures in this manuscript will be made available via a DASH repository upon publication: https://data.ucar.edu/. All observational datasets used for model validation are publicly available.

Further details on the model setup can be found at https://github.com/mnlevy1981/frontera_highres/tree/main. The Python-based FEISTY code used in this study can be found here: https://github.com/marbl-ecosys/feisty

7 Acknowledgements

This material is based upon work supported by the National Science Foundation (NSF) National Center for Atmospheric Research, which is a major facility sponsored by the U.S. National Science Foundation under Cooperative Agreement No. 1852977. We are grateful for funding from National Aeronautics and Space Administration (NASA; grant number 80NSSC20K1289, Project number 19-IDS19-0028). The authors acknowledge NSF Convergence Accelerator Track E grant 2137684, NSF AGS-2231237, NSF OCE-1735846 and NSF OCE-1948718. This research was supported by NOAA's Climate Program Office's Modeling, Analysis, Predictions, and Projections (MAPP) program, grants NA20OAR4310441 and NA20OAR4310442, and through participation in the MAPP Marine Ecosystem Task Force. The authors acknowledge the Texas Advanced Computing Center (TACC) for providing HPC resources on Frontera that have contributed to the research results reported here (FOSI-HR simulation). The authors also acknowledge high-performance computing support from Cheyenne (doi:10.5065/D6RX99HX) provided by NCAR's Computational and Information Systems Laboratory, sponsored by the National Science Foundation (FOSI-LR simulation).

8 Declaration of competing interest

The authors declare no competing interests.

References

Andersen, K. H., Farnsworth, K., Pedersen, M., Gislason, H., & Beyer, J. (2009). How community ecology links natural mortality, growth, and production of fish populations. *ICES Journal of Marine Science*, *66*(9), 1978–1984.

Andersen, K. (2019). Size spectrum theory. *Fish ecology, evolution, and exploitation: a new theoretical synthesis. Princeton University Press, New Jersey*, 15–37.

Armstrong, R. A., Lee, C., Hedges, J. I., Honjo, S., & Wakeham, S. G. (2001). A new, mechanistic model for organic carbon fluxes in the ocean based on the quantitative association of poc with ballast minerals [The US JGOFS Synthesis and Modeling Project: Phase 1]. *Deep Sea Research Part II: Topical Studies in Oceanography*, *49*(1), 219–236. https://doi.org/10.1016/S0967-0645(01)00101-1

Arrigo, K. R., van Dijken, G. L., & Bushinsky, S. (2008). Primary production in the southern ocean, 1997–2006. *Journal of Geophysical Research: Oceans*, *113*(C8). https://doi.org/10.1029/2007JC004551

Balch, W. M., Gordon, H. R., Bowler, B. C., Drapeau, D. T., & Booth, E. S. (2005). Calcium carbonate measurements in the surface global ocean based on moderate-resolution imaging spectroradiometer data. *Journal of Geophysical Research: Oceans*, *110*(C7). https://doi.org/10.1029/2004JC002560

Balch, W. M. (2018). The ecology, biogeochemistry, and optical properties of coccolithophores. *Annual Review of Marine Science*, *10*(1), 71–98. https://doi.org/10.1146/annurev-marine-121916-063319

Behrenfeld, M. J., Boss, E., Siegel, D. A., & Shea, D. M. (2005). Carbon-based ocean productivity and phytoplankton physiology from space. *Global Biogeochem. Cycles*, *19*(1). https://doi.org/10.1029/2004GB002299

Behrenfeld, M. J., & Boss, E. S. (2014). Resurrecting the ecological underpinnings of ocean plankton blooms. *Annual Review of Marine Science*, *6*(1), 167–194. https://doi.org/10.1146/annurev-marine-052913-021325

Behrenfeld, M. J., & Falkowski, P. G. (1997). Photosynthetic rates derived from satellite-based chlorophyll concentration. *Limnology and Oceanography*, *42*(1), 1–20. https://doi.org/10.4319/lo.1997.42.1.0001

Bemal, S., & Anil, A. C. (2019). Picophytoplankton synechococcus as food for nauplii of amphibalanus amphitrite and artemia salina. *Hydrobiologia*, *835*(1), 21–36. https://doi.org/10.1007/s10750-019-3923-x

Bianchi, D., Carozza, D. A., Galbraith, E. D., Guiet, J., & DeVries, T. (2021). Estimating global biomass and biogeochemical cycling of marine fish with and without fishing. *Science Advances*, *7*(41), eabd7554. https://doi.org/10.1126/sciadv.abd7554

Bianchi, D., Stock, C., Galbraith, E. D., & Sarmiento, J. L. (2013). Diel vertical migration: Ecological controls and impacts on the biological pump in a one-dimensional ocean model. *Global Biogeochemical Cycles*, *27*(2), 478–491. https://doi.org/https://doi.org/10.1002/gbc.20031

Bopp, L., Resplandy, L., Orr, J. C., Doney, S. C., Dunne, J. P., Gehlen, M., Halloran, P., Heinze, C., Ilyina, T., Séférian, R., Tjiputra, J., & Vichi, M. (2013). Multiple stressors of ocean ecosystems in the 21st century: Projections with cmip5 models. *Biogeosciences*, *10*(10), 6225–6245. https://doi.org/10.5194/bg-10-6225-2013

Buitenhuis, E. T., Rivkin, R. B., Sailley, S., & Le Quéré, C. (2010). Biogeochemical fluxes through microzooplankton. *Global Biogeochemical Cycles*, *24*(4). https://doi.org/10.1029/2009GB003601

Carr, M.-E., Friedrichs, M. A., Schmeltz, M., Noguchi Aita, M., Antoine, D., Arrigo, K. R., Asanuma, I., Aumont, O., Barber, R., Behrenfeld, M., Bidigare, R., Buitenhuis, E. T., Campbell, J., Ciotti, A., Dierssen, H., Dowell, M., Dunne, J., Esaias, W., Gentili, B., ... Yamanaka, Y. (2006). A comparison of global estimates of marine primary production from ocean color [The US JGOFS Synthesis and Modeling Project: Phase III]. *Deep Sea Research Part II: Topical Studies in Oceanography*, *53*(5), 741–770. https://doi.org/10.1016/j.dsr2.2006.01.028

Chang, P., Xu, G., Kurian, J., Small, R. J., Danabasoglu, G., Yeager, S., Castruccio, F., Zhang, Q., Rosenbloom, N., & Chapman, P. (2023). Uncertain future of sustainable fisheries environment in eastern boundary upwelling zones under climate change. *Communications Earth & Environment*, *4*(19). https://doi.org/10.1038/s43247-023-00681-0

Chang, P., Zhang, S., Danabasoglu, G., Yeager, S. G., Fu, H., Wang, H., Castruccio, F. S., Chen, Y., Edwards, J., Fu, D., Jia, Y., Laurindo, L. C., Liu, X., Rosenbloom, N., Small, R. J., Xu, G., Zeng, Y., Zhang, Q., Bacmeister, J., ... Wu, L. (2020). An unprecedented set of high-resolution earth system simulations for understanding multiscale interactions in climate variability and change. *Journal of Advances in Modeling Earth Systems*, *12*(12). https://doi.org/10.1029/2020MS002298

Chassignet, E. P., Yeager, S. G., Fox-Kemper, B., Bozec, A., Castruccio, F., Danabasoglu, G., Horvat, C., Kim, W. M., Koldunov, N., Li, Y., Lin, P., Liu, H., Sein, D. V., Sidorenko, D., Wang, Q., & Xu, X. (2020). Impact of horizontal resolution on global ocean–sea ice model simulations based on the experimental protocols of the Ocean Model Intercomparison Project phase 2 (OMIP-2). *Geoscientific Model Development*, *13*(9), 4595–4637. https://doi.org/10.5194/gmd-13-4595-2020

Cheng, L., Trenberth, K. E., Fasullo, J., Boyer, T., Abraham, J., & Zhu, J. (2017). Improved estimates of ocean heat content from 1960 to 2015. *Science Advances*, *3*(3), e1601545. https://doi.org/10.1126/sciadv.1601545

Clerc, C., Aumont, O., & Bopp, L. (2023). Filter-feeding gelatinous macrozooplankton response to climate change and implications for benthic food supply and global carbon cycle. *Global Change Biology*, *29*(22), 6383–6398. https://doi.org/https://doi.org/10.1111/gcb.16942

COML. (2010). Census of Marine Life. http://coml.org

Danabasoglu, G., Lamarque, J.-F., Bacmeister, J., Bailey, D. A., DuVivier, A. K., Edwards, J., Emmons, L. K., Fasullo, J., Garcia, R., Gettelman, A., Hannay, C., Holland, M. M., Large, W. G., Lauritzen, P. H., Lawrence, D. M., Lenaerts, J. T. M., Lindsay, K., Lipscomb, W. H., Mills, M. J., ... Strand, W. G. (2020). The community earth system model version 2 (cesm2) [e2019MS001916 2019MS001916]. *Journal of Advances in Modeling Earth Systems*, *12*(2), e2019MS001916. https://doi.org/10.1029/2019MS001916

Danabasoglu, G., Yeager, S. G., Kwon, Y.-O., Tribbia, J. J., Phillips, A. S., & Hurrell, J. W. (2012). Variability of the atlantic meridional overturning circulation in ccsm4. *Journal of Climate*, *25*(15), 5153–5172. https://doi.org/10.1175/JCLI-D-11-00463.1

Deppeler, S. L., & Davidson, A. T. (2017). Southern ocean phytoplankton in a changing climate. *Frontiers in Marine Science*, *4*. https://doi.org/10.3389/fmars.2017.00040

DeVries, T., & Weber, T. (2017). The export and fate of organic matter in the ocean: New constraints from combining satellite and oceanographic tracer observations. *Global Biogeochemical Cycles*, *31*(3), 535–555. https://doi.org/10.1002/2016GB005551

Di Lorenzo, E., & Mantua, N. (2016). Multi-year persistence of the 2014/15 north pacific marine heatwave. *Nature Climate Change*, *6*, 1042–1047. https://doi.org/10.1038/nclimate3082

Doney, S. C., Lindsay, K., Fung, I., & John, J. (2006). Natural variability in a stable, 1000-yr global coupled climate–carbon cycle simulation. *Journal of Climate*, *19*(13), 3033–3054. https://doi.org/10.1175/JCLI3783.1

Dugdale, R. C., & Goering, J. J. (1967). Uptake of new and regenerated forms of nitrogen in primary productivity. *Limnology and Oceanography*, *12*(2), 196–206. https://doi.org/10.4319/lo.1967.12.2.0196

Dupont, L., Le Mézo, P., Aumont, O., Bopp, L., Clerc, C., Ethé, C., & Maury, O. (2023). High trophic level feedbacks on global ocean carbon uptake and marine ecosystem dynamics under climate change. *Global Change Biology*, *29*(6), 1545–1556. https://doi.org/https://doi.org/10.1111/gcb.16558

Eddebbar, Y., Subramanian, A., Whitt, D., Long, M., Verdy, A., Mazloff, M., & Merrifield, M. (2021). Seasonal modulation of dissolved oxygen in the equatorial pacific by tropical instability vortices. *Journal of Geophysical Research: Oceans*, *126*(11), e2021JC017567.

Edwards, A. M., & Yool, A. (2000). The role of higher predation in plankton population models. *Journal of Plankton Research*, *22*(6), 1085–1112. https://doi.org/10.1093/plankt/22.6.1085

FAO. (2018). *The State of World Fisheries and Aquaculture 2018 - Meeting the sustainable development goals (Report No. ISBN 978-92-5-130562-1)* (tech. rep.). Food and Agriculture Organization.

Fasham, M. (1995). Variations in the seasonal cycle of biological production in subarctic oceans: A model sensitivity analysis. *Deep Sea Research Part I: Oceanographic Research Papers*, *42*(7), 1111–1149. https://doi.org/10.1016/0967-0637(95)00054-A

Fetterer, F., Knowles, K., Meier, W. N., Savoie, M., & Windnagel, A. K. (2017). *Sea ice index, version 3* (tech. rep.) [(accessed June 2, 2023)]. National Snow and Ice Data Center, Boulder, Colorado, U.S.A. https://doi.org/10.7265/N5K072F8

Field, C. B., Behrenfeld, M. J., Randerson, J. T., & Falkowski, P. (1998). Primary production of the biosphere: Integrating terrestrial and oceanic components. *Science*, *281*(5374), 237–240. https://doi.org/10.1126/science.281.5374.237

Fielding, S. R. (2013). Emiliania huxleyi specific growth rate dependence on temperature. *Limnology and Oceanography*, *58*(2), 663–666. https://doi.org/10.4319/lo.2013.58.2.0663

Flores, H., Veyssiere, G., Castellani, G., Wilkinson, J., Hoppmann, M., Karcher, M., Valcic, L., Cornils, A., Geoffroy, M., Nicolaus, M., Niehoff, B., Priou, P., Schmidt, K., & Stroeve, J. (2023). Sea-ice decline could keep zooplankton deeper for longer. *Nature Climate Change*. https://doi.org/10.1038/s41558-023-01779-1

Follows, M. J., Dutkiewicz, S., Grant, S., & Chisholm, S. W. (2007). Emergent biogeography of microbial communities in a model ocean. *Science*, *315*(5820), 1843–1846. https://doi.org/10.1126/science.1138544

Friedland, K. D., Record, N. R., Asch, R. G., Kristiansen, T., Saba, V. S., Drinkwater, K. F., Henson, S., Leaf, R. T., Morse, R. E., Johns, D. G., Large, S. I., Hjøllo, S. S., Nye, J. A., Alexander, M. A., & Ji, R. (2016). Seasonal phytoplankton blooms in the north atlantic linked to the overwintering strategies of copepods [000099]. *Elementa: Science of the Anthropocene*, *4*. https://doi.org/10.12952/journal.elementa.000099

Friedlingstein, P., Cox, P., Betts, R., Bopp, L., von Bloh, W., Brovkin, V., Cadule, P., Doney, S., Eby, M., Fung, I., Bala, G., John, J., Jones, C., Joos, F., Kato, T., Kawamiya, M., Knorr, W., Lindsay, K., Matthews, H. D., … Zeng, N. (2006). Climate–carbon cycle feedback analysis: Results from the c4mip model intercomparison. *Journal of Climate*, *19*(14), 3337–3353. https://doi.org/10.1175/JCLI3800.1

Friedlingstein, P., O'Sullivan, M., Jones, M. W., Andrew, R. M., Gregor, L., Hauck, J., Le Quéré, C., Luijkx, I. T., Olsen, A., Peters, G. P., Peters, W., Pongratz, J., Schwingshackl, C., Sitch, S., Canadell, J. G., Ciais, P., Jackson, R. B., Alin, S. R., Alkama, R., … Zheng, B. (2022). Global carbon budget 2022. *Earth System Science Data*, *14*(11), 4811–4900. https://doi.org/10.5194/essd-14-4811-2022

Garcia, H. E., Weathers, K., Paver, C. R., Smolyar, I., Boyer, T. P., Locarnini, R. A., Zweng, M. M., Mishonov, A. V., Baranova, O. K., Seidov, D., & Reagan, J. R. (2018). *World Ocean Atlas 2018, Volume 4: Dissolved inorganic nutrients (phosphate, nitrate and nitrate+nitrite, silicate)* (Vol. NOAA Atlas NESDIS 84). U.S. Department of Commerce.

Garnesson, P., Mangin, A., Fanton d'Andon, O., Demaria, J., & Bretagnon, M. (2019). The cmems globcolour chlorophyll *a* product based on satellite observation: Multi-sensor merging and flagging strategies. *Ocean Science*, *15*(3), 819–830. https://doi.org/10.5194/os-15-819-2019

Geider, R. J., MacIntyre, H. L., & Kana, T. M. (1997). Dynamic model of phytoplankton growth and acclimation: Responses of the balanced growth rate and the chlorophyll a:carbon ratio to light, nutrient-limitation and temperature. *Marine Ecology Progress Series*, *148*, 187–200. https://www.int-res.com/abstracts/meps/v148/p187-200/

Godø, O. R., Samuelsen, A., Macaulay, G. J., Patel, R., Hjøllo, S. S., Horne, J., Kaartvedt, S., & Johannessen, J. A. (2012). Mesoscale eddies are oases for higher trophic marine life. *PLOS ONE*, *7*(1), 1–9. https://doi.org/10.1371/journal.pone.0030161

Gruber, N. (2011). Warming up, turning sour, losing breath: Ocean biogeochemistry under global change. *Philosophical Transactions of the Royal Society A: Mathematical, Physical and Engineering Sciences*, *369*(1943), 1980–1996. https://doi.org/10.1098/rsta.2011.0003

Gruber, N., Lachkar, Z., Frenzel, H., Marchesiello, P., Münnich, M., McWilliams, J. C., & Plattner, G.-K. (2011). Eddy-induced reduction of biological production in eastern boundary upwelling systems. *Nature Geoscience*, *4*, 787–792. https://doi.org/10.1038/ngeo1273

Haberman, K. L., Ross, R. M., & Quetin, L. B. (2003). Diet of the antarctic krill (euphausia superba dana): Ii. selective grazing in mixed phytoplankton assemblages. *Journal of Experimental Marine Biology and Ecology*, *283*(1), 97–113. https://doi.org/10.1016/S0022-0981(02)00467-7

Halpern, D., Knox, R. A., & Luther, D. S. (1988). Observations of 20-day period meridional current oscillations in the upper ocean along the pacific equator. *Journal of Physical Oceanography*, *18*(11), 1514–1534.

Hanchet, S., Dunn, A., Parker, S., Horn, P., Stevens, D., & Mormede, S. (2015). The antarctic toothfish (dissostichus mawsoni): Biology, ecology, and life history in the ross sea region. *Hydrobiologia*. https://doi.org/10.1007/s10750-015-2435-6

Hansen, P. J., Bjørnsen, P. K., & Hansen, B. W. (1997). Zooplankton grazing and growth: Scaling within the 2-2000-μm body size range. *Limnology and Oceanography*, *42*(4), 687–704. https://doi.org/10.4319/lo.1997.42.4.0687

Harrison, C. S., Long, M. C., Lovenduski, N. S., & Moore, J. K. (2018). Mesoscale effects on carbon export: A global perspective. *Global Biogeochemical Cycles*, *32*(4), 680–703. https://doi.org/10.1002/2017GB005751

Hatton, I. A., Heneghan, R. F., Bar-On, Y. M., & Galbraith, E. D. (2021). The global ocean size spectrum from bacteria to whales. *Science Advances*, *7*(46), eabh3732. https://doi.org/10.1126/sciadv.abh3732

Haunost, M., Riebesell, U., D'Amore, F., Kelting, O., & Bach, L. T. (2021). Influence of the calcium carbonate shell of coccolithophores on ingestion and growth of a dinoflagellate predator. *Frontiers in Marine Science*, *8*. https://doi.org/10.3389/fmars.2021.664269

Heneghan, R. F., Everett, J. D., Blanchard, J. L., Sykes, P., & Richardson, A. J. (2023). Climate-driven zooplankton shifts cause large-scale declines in food quality for fish. *Nature Climate Change*, *13*, 470–477. https://doi.org/10.1038/s41558-023-01630-7

Heneghan, R. F., Galbraith, E., Blanchard, J. L., Harrison, C., Barrier, N., Bulman, C., Cheung, W., Coll, M., Eddy, T. D., Erauskin-Extramiana, M., Everett, J. D., Fernandes-Salvador, J. A., Gascuel, D., Guiet, J., Maury, O., Palacios-Abrantes, J., Petrik, C. M., du Pontavice, H., Richardson, A. J., ... Tittensor, D. P. (2021). Disentangling diverse responses to climate change among global marine ecosystem models. *Progress in Oceanography*, *198*, 102659. https://doi.org/10.1016/j.pocean.2021.102659

Holzer, M., Primeau, F. W., DeVries, T., & Matear, R. (2014). The southern ocean silicon trap: Data-constrained estimates of regenerated silicic acid, trapping efficiencies, and global transport paths. *Journal of Geophysical Research: Oceans*, *119*(1), 313–331. https://doi.org/10.1002/2013JC009356

Hunke, E. C., Lipscomb, W. H., Turner, A. K., Jeffery, N., & Elliot, S. (2015). *CICE: The Los Alamos Sea Ice Model. Documentation and software user's manual. Version 5.1* (tech. rep.). Los Alamos National Laboratory, LA-CC-06-012.

Irigoien, X., Harris, R. P., Verheye, H. M., Joly, P., Runge, J., Starr, M., Pond, D., Campbell, R., Shreeve, R., Ward, P., Smith, A. N., Dam, H. G., Peterson, W., Tirelli, V., Koski, M., Smith, T., Harbour, D., & Davidson, R. (2002). Copepod hatching success in marine ecosystems with high diatom concentrations. *Nature*, *419*(6905), 387–389. https://doi.org/10.1038/nature01055

Jennings, S., & Collingridge, K. (2015). Predicting consumer biomass, size-structure, production, catch potential, responses to fishing and associated uncertainties in the world's marine ecosystems. *PLOS ONE*, *10*(7), 1–28. https://doi.org/10.1371/journal.pone.0133794

Jenouvrier, S., Che-Castaldo, J., Wolf, S., Holland, M., Labrousse, S., LaRue, M., Wienecke, B., Fretwell, P., Barbraud, C., Greenwald, N., Stroeve, J., & Trathan, P. N. (2021). The call of the emperor penguin: Legal responses to species threatened by climate change. *Global Change Biology*, *27*(20), 5008–5029. https://doi.org/10.1111/gcb.15806

Kiørboe, T., Visser, A., & Andersen, K. H. (2018). A trait-based approach to ocean ecology. *ICES Journal of Marine Science*, *75*(6), 1849–1863.

Kirtman, B. P., Bitz, C., Bryan, F., Collins, W., Dennis, J., Hearn, N., Kinter, J. L., Loft, R., Rousset, C., Siqueira, L., Stan, C., Tomas, R., & Vertenstein, M. (2012). Impact of ocean model resolution on CCSM climate simulations. *Climate Dynamics*, *39*(6), 1303–1328. https://doi.org/10.1007/s00382-012-1500-3

Kobayashi, S., Ota, Y., Haradoa, Y., Ebita, A., Moriya, M., Onoda, H., Onogi, K., Kamahori, H., Kobayashi, C., Endo, H., Miyaoka, K., & Takahashi, K. (2015). The JRA-55 reanalysis: General specifications and basic characteristics. *Journal of the Meteorological Society of Japan. Ser. II*, *93*(1), 5–48. https://doi.org/10.2151/jmsj.2015-001

Krumhardt, K. M., Long, M. C., Lindsay, K., & Levy, M. N. (2020). Southern ocean calcification controls the global distribution of alkalinity [e2020GB006727 10.1029/2020GB006727]. *Global Biogeochemical Cycles*, *34*(12), e2020GB006727. https://doi.org/10.1029/2020GB006727

Krumhardt, K. M., Lovenduski, N. S., Long, M. C., Levy, M., Lindsay, K., Moore, J. K., & Nissen, C. (2019). Coccolithophore growth and calcification in an acidified ocean: Insights from community earth system model simulations. *Journal of Advances in Modeling Earth Systems*, *11*(5), 1418–1437. https://doi.org/10.1029/2018MS001483

Krumhardt, K. M., Lovenduski, N. S., Iglesias-Rodriguez, M. D., & Kleypas, J. A. (2017). Coccolithophore growth and calcification in a changing ocean. *Progress in Oceanography*, *159*, 276–295. https://doi.org/10.1016/j.pocean.2017.10.007

Landry, M. R., & Calbet, A. (2004). Microzooplankton production in the oceans. *ICES Journal of Marine Science*, *61*(4), 501–507. https://doi.org/10.1016/j.icesjms.2004.03.011

Legeckis, R. (1977). Long waves in the eastern equatorial pacific ocean: A view from a geostationary satellite. *Science*, *197*(4309), 1179–1181.

Lehodey, P., Alheit, J., Barange, M., Baumgartner, T., Beaugrand, G., Drinkwater, K., Fromentin, J.-M., Hare, S. R., Ottersen, G., Perry, R. I., Roy, C., van der Lingen, C. D., & Werner, F. (2006). Climate variability, fish, and fisheries. *Journal of Climate*, *19*(20), 5009–5030. https://doi.org/10.1175/JCLI3898.1

Liang, H., Lunstrum, A. M., Dong, S., Berelson, W. M., & John, S. G. (2023). Constraining caco3 export and dissolution with an ocean alkalinity inverse model [e2022GB007535 2022GB007535]. *Global Biogeochemical Cycles*, *37*(2), e2022GB007535. https://doi.org/10.1029/2022GB007535

Long, M. C., Moore, J. K., Lindsay, K., Levy, M., Doney, S. C., Luo, J. Y., Krumhardt, K. M., Letscher, R. T., Grover, M., & Sylvester, Z. T. (2021). Simulations with the marine biogeochemistry library (MARBL). *Journal of Advances in Modeling Earth Systems*, *13*(12), e2021MS002647. https://doi.org/10.1029/2021MS002647

Lotze, H. K., Tittensor, D. P., Bryndum-Buchholz, A., Eddy, T. D., Cheung, W. W. L., Galbraith, E. D., Barange, M., Barrier, N., Bianchi, D., Blanchard, J. L., Bopp, L., Büchner, M., Bulman, C. M., Carozza, D. A., Christensen, V., Coll, M., Dunne, J. P., Fulton, E. A., Jennings, S., ... Worm, B. (2019). Global ensemble projections reveal trophic amplification of ocean biomass declines with climate change. *Proceedings of the National Academy of Sciences*, *116*(26), 12907–12912. https://doi.org/10.1073/pnas.1900194116

Luo, J. Y., Stock, C. A., Henschke, N., Dunne, J. P., & O'Brien, T. D. (2022). Global ecological and biogeochemical impacts of pelagic tunicates. *Progress in Oceanography*, *205*, 102822. https://doi.org/https://doi.org/10.1016/j.pocean.2022.102822

Macias-Fauria, M., & Post, E. (2018). Effects of sea ice on arctic biota: An emerging crisis discipline. *Biology Letters*, *14*(3), 20170702. https://doi.org/10.1098/rsbl.2017.0702

Mahadevan, A., D'Asaro, E., Lee, C., & Perry, M. J. (2012). Eddy-driven stratification initiates north atlantic spring phytoplankton blooms. *Science*, *337*(6090), 54–58. https://doi.org/10.1126/science.1218740

Maury, O. (2010). An overview of apecosm, a spatialized mass balanced "apex predators ecosystem model" to study physiologically structured tuna population dynamics in their ecosystem. *Progress in Oceanography*, *84*(1-2), 113–117.

Mayorga, E., Seitzinger, S. P., Harrison, J. A., Dumont, E., Beusen, A. H., Bouwman, A., Fekete, B. M., Kroeze, C., & Van Drecht, G. (2010). Global nutrient export from watersheds 2 (news 2): Model development and implementation. *Environmental Modelling & Software*, *25*(7), 837–853. https://doi.org/10.1016/j.envsoft.2010.01.007

McGillicuddy, D. J. (2016). Mechanisms of physical-biological-biogeochemical interaction at the oceanic mesoscale. *Annual Review of Marine Science*, *8*, 125–159. https://doi.org/https://doi.org/10.1146/annurev-marine-010814-015606

Meier, W. N., Fetterer, F., Windnagel, A. K., & Stewart, J. S. (2021). *Noaa/nsidc climate data record of passive microwave sea ice concentration, version 4. southern hemisphere, 1979-2020* (tech. rep.) [(accessed July 11, 2023)]. National Snow and Ice Data Center, Boulder, Colorado, U.S.A. https://doi.org/10.7265/efmz-2t65

Miller, L., Watts, D. R., & Wimbush, M. (1985). Oscillations of dynamic topography in the eastern equatorial pacific. *Journal of physical oceanography*, *15*(12), 1759–1770.

Moeller, H. V., Laufkötter, C., Sweeney, E. M., & Johnson, M. D. (2019). Light-dependent grazing can drive formation and deepening of deep chlorophyll maxima. *Nature Communications*, *10*, 1978. https://doi.org/10.1038/s41467-019-09591-2

Mogen, S. C., Lovenduski, N. S., Dallmann, A. R., Gregor, L., Sutton, A. J., Bograd, S. J., Quiros, N. C., Di Lorenzo, E., Hazen, E. L., Jacox, M. G., Buil, M. P., & Yeager, S. (2022). Ocean biogeochemical signatures of the north pacific blob. *Geophysical Research Letters*, *49*(9), e2021GL096938. https://doi.org/10.1029/2021GL096938

Moore, J. K., Lindsay, K., Doney, S. C., Long, M. C., & Misumi, K. (2013). Marine ecosystem dynamics and biogeochemical cycling in the Community Earth System Model [CESM1(BGC)]: Comparison of the 1990s with the 2090s under the RCP4.5 and RCP8.5 scenarios. *Journal of Climate*, *26*(23), 9291–9312. https://doi.org/10.1175/JCLI-D-12-00566.1

Moriarty, R., & O'Brien, T. D. (2013). Distribution of mesozooplankton biomass in the global ocean. *Earth System Science Data*, *5*(1), 45–55. https://doi.org/10.5194/essd-5-45-2013

Nejstgaard, J., Gismervik, I., & Solberg, P. (1997). Feeding and reproduction by calanus finmarchicus, and microzooplankton grazing during mesocosm blooms of diatoms and the coccolithophore emiliania huxleyi. *Marine Ecology Progress Series*, *147*, 197–217. https://www.int-res.com/abstracts/meps/v147/p197-217/

Nelson, D. M., Tréguer, P., Brzezinski, M. A., Leynaert, A., & Quéguiner, B. (1995). Production and dissolution of biogenic silica in the ocean: Revised global estimates, comparison with regional data and relationship to biogenic sedimentation. *Global Biogeochemical Cycles*, *9*(3), 359–372. https://doi.org/10.1029/95GB01070

NMFS. (2018). *Fisheries Economics of the United States* (tech. rep.). National Marine Fisheries Service, U. S. Dept. of Commerce, NOAA Tech. Memo. NMFS-F/SPO-187, 243 P.

Noh, K. M., Lim, H.-G., & Kug, J.-S. (2022). Global chlorophyll responses to marine heatwaves in satellite ocean color. *Environmental Research Letters*, *17*(6), 064034. https://doi.org/10.1088/1748-9326/ac70ec

Ohman, M. D., & Hirche, H.-J. (2001). Density-dependent mortality in an oceanic copepod population. *Nature*, *412*, 638–641. https://doi.org/10.1038/35088068

Olsson, K. H., & Gislason, H. (2016). Testing reproductive allometry in fish. *ICES Journal of Marine Science*, *73*(6), 1466–1473.

Palter, J. B. (2015). The role of the gulf stream in european climate. *Annual Review of Marine Science*, *7*(Volume 7, 2015), 113–137. https://doi.org/https://doi.org/10.1146/annurev-marine-010814-015656

Pauly, D., Zeller, D., & Palomares, M. L. D. (2020). *Sea around us concepts, design, and data*. www.seaaroundus.org.

Penn, J. L., & Deutsch, C. (2022). Avoiding ocean mass extinction from climate warming. *Science*, *376*(6592), 524–526. https://doi.org/10.1126/science.abe9039

Petrik, C. M., Stock, C. A., Andersen, K. H., van Denderen, P. D., & Watson, J. R. (2019). Bottom-up drivers of global patterns of demersal, forage, and pelagic fishes. *Progress in Oceanography*, *176*, 102124. https://doi.org/10.1016/j.pocean.2019.102124

Petrik, C. M., Stock, C. A., Andersen, K. H., van Denderen, P. D., & Watson, J. R. (2020). Large pelagic fish are most sensitive to climate change despite pelagification of ocean food webs. *Frontiers in Marine Science*, *7*. https://doi.org/10.3389/fmars.2020.588482

Pinti, J., Andersen, K. H., & Visser, A. W. (2021). Co-adaptive behavior of interacting populations in a habitat selection game significantly impacts ecosystem functions. *Journal of Theoretical Biology*, *523*, 110663. https://doi.org/https://doi.org/10.1016/j.jtbi.2021.110663

Qiao, L., & Weisberg, R. H. (1995). Tropical instability wave kinematics: Observations from the tropical instability wave experiment. *Journal of Geophysical Research: Oceans*, *100*(C5), 8677–8693.

Roach, L. A., Dörr, J., Holmes, C. R., Massonnet, F., Blockley, E. W., Notz, D., Rackow, T., Raphael, M. N., O'Farrell, S. P., Bailey, D. A., & Bitz, C. M. (2020). Antarctic sea ice area in cmip6 [e2019GL086729 10.1029/2019GL086729]. *Geophysical Research Letters*, *47*(9), e2019GL086729. https://doi.org/https://doi.org/10.1029/2019GL086729

Rousseaux, C. S., & Gregg, W. W. (2012). Climate variability and phytoplankton composition in the Pacific Ocean. *Journal of Geophysical Research: Oceans*, *117*(C10). https://doi.org/https://doi.org/10.1029/2012JC008083

Ryther, J. H. (1969). Photosynthesis and fish production in the sea. *Science*, *166*(3901), 72–76. Retrieved April 5, 2023, from http://www.jstor.org/stable/1727735

Saba, V. S., Friedrichs, M. A. M., Antoine, D., Armstrong, R. A., Asanuma, I., Behrenfeld, M. J., Ciotti, A. M., Dowell, M., Hoepffner, N., Hyde, K. J. W., Ishizaka, J., Kameda, T., Marra, J., Mélin, F., Morel, A., O'Reilly, J., Scardi, M., Smith Jr., W. O., Smyth, T. J., ... Westberry, T. K. (2011). An evaluation of ocean color model estimates of marine primary productivity in coastal and pelagic regions across the globe. *Biogeosciences*, *8*(2), 489–503. https://doi.org/10.5194/bg-8-489-2011

Schubert, R., Thompson, A. F., Speer, K., Schulze Chretien, L., & Bebieva, Y. (2021). The antarctic coastal current in the bellingshausen sea. *The Cryosphere*, *15*(9), 4179–4199. https://doi.org/10.5194/tc-15-4179-2021

Sharp, J. D., Fassbender, A. J., Carter, B. R., Johnson, G. C., Schultz, C., & Dunne, J. P. (2022). *GOBAI-O_2: A global gridded monthly dataset of ocean interior dissolved oxygen concentrations based on shipboard and autonomous observations (ncei accession 0259304)* (tech. rep.). NOAA National Centers for Environmental Information. https://doi.org/10.25921/z72m-yz67

Sherman, E., Moore, J. K., Primeau, F., & Tanouye, D. (2016). Temperature influence on phytoplankton community growth rates. *Global biogeochemical cycles*, *30*(4), 550–559. https://doi.org/10.1002/2015gb005272

Sherman, K., Belkin, I. M., Friedland, K. D., O'Reilly, J., & Hyde, K. (2009). Accelerated Warming and Emergent Trends in Fisheries Biomass Yields of the World's Large Marine Ecosystems. *AMBIO: A Journal of the Human Environment*, *38*(4), 215–224. https://doi.org/10.1579/0044-7447-38.4.215

Small, R. J., Kurian, J., Chang, P., Xu, G., Tsujino, H., Yeager, S., Danabasoglu, G., Kim, W. M., Altuntas, A., & Castruccio, F. (2024). Eastern boundary upwelling systems in ocean–sea ice simulations forced by core and jra55-do: Mean state and variability at the surface. *Journal of Climate*, *37*(9), 2821–2848. https://doi.org/10.1175/JCLI-D-23-0511.1

Smetacek, V., Klaas, C., Menden-Deuer, S., & Rynearson, T. A. (2002). Mesoscale distribution of dominant diatom species relative to the hydrographical field along the antarctic polar front [Mesoscale Physics, Biogeochemistry and Ecology of the Antarctic Polar Front, Atlantic Sector]. *Deep Sea Research Part II: Topical Studies in Oceanography*, *49*(18), 3835–3848. https://doi.org/10.1016/S0967-0645(02)00113-3

Smith, R. D., Jones, P., Briegleb, B., Bryan, F., Danabasoglu, G., Dennis, J., Dukowicz, J., Eden, C., Fox-Kemper, B., Gent, P., Hecht, M., Jayne, S., Jocham, M., Large, W., Lindsay, K., Maltrud, M., Norton, N., Peacock, S., Vertenstein, M., & Yeager, S. (2010). *The parallel ocean program (POP) reference manual* (tech. rep.). Los Alamos National Laboratory, LAUR-10-01853.

Song, H., Long, M. C., Gaube, P., Frenger, I., Marshall, J., & McGillicuddy Jr., D. J. (2018). Seasonal variation in the correlation between anomalies of sea level and chlorophyll in the antarctic circumpolar current. *Geophysical Research Letters*, *45*(10), 5011–5019. https://doi.org/10.1029/2017GL076246

Stammer, D. (1997). Global characteristics of ocean variability estimated from regional topex/poseidon altimeter measurements. *Journal of Physical Oceanography*, *27*(8), 1743–1769. https://journals.ametsoc.org/view/journals/phoc/27/8/1520-0485_1997_027_1743_gcoove_2.0.co_2.xml

Steele, J. H., & Henderson, E. W. (1992). The role of predation in plankton models. *Journal of Plankton Research*, *14*(1), 157–172. https://doi.org/10.1093/plankt/14.1.157

Stock, C. A., Dunne, J. P., & John, J. G. (2014a). Drivers of trophic amplification of ocean productivity trends in a changing climate. *Biogeosciences*, *11*(24), 7125–7135. https://doi.org/10.5194/bg-11-7125-2014

Stock, C. A., Alexander, M. A., Bond, N. A., Brander, K. M., Cheung, W. W., Curchitser, E. N., Delworth, T. L., Dunne, J. P., Griffies, S. M., Haltuch, M. A., Hare, J. A., Hollowed, A. B., Lehodey, P., Levin, S. A., Link, J. S., Rose, K. A., Rykaczewski, R. R., Sarmiento, J. L., Stouffer, R. J., … Werner, F. E. (2011). On the use of ipcc-class models to assess the impact of climate on living marine resources. *Progress in Oceanography*, *88*(1), 1–27. https://doi.org/10.1016/j.pocean.2010.09.001

Stock, C. A., Dunne, J. P., & John, J. G. (2014b). Global-scale carbon and energy flows through the marine planktonic food web: An analysis with a coupled physical–biological model. *Progress in Oceanography*, *120*, 1–28. https://doi.org/10.1016/j.pocean.2013.07.001

Stock, C. A., John, J. G., Rykaczewski, R. R., Asch, R. G., Cheung, W. W. L., Dunne, J. P., Friedland, K. D., Lam, V. W. Y., Sarmiento, J. L., & Watson, R. A. (2017). Reconciling fisheries catch and ocean productivity. *Proceedings of the National Academy of Sciences*, *114*(8), E1441–E1449. https://doi.org/10.1073/pnas.1610238114

Straile, D. (1997). Gross growth efficiencies of protozoan and metazoan zooplankton and their dependence on food concentration, predator-prey weight ratio, and taxonomic group. *Limnology and Oceanography*, *42*(6), 1375–1385. https://doi.org/10.4319/lo.1997.42.6.1375

Tommasi, D., Stock, C. A., Hobday, A. J., Methot, R., Kaplan, I. C., Eveson, J. P., Holsman, K., Miller, T. J., Gaichas, S., Gehlen, M., Pershing, A., Vecchi, G. A., Msadek, R., Delworth, T., Eakin, C. M., Haltuch, M. A., Séférian, R., Spillman, C. M., Hartog, J. R., … Werner, F. E. (2017). Managing living marine resources in a dynamic environment: The role of seasonal to decadal climate forecasts. *Progress in Oceanography*, *152*, 15–49. https://doi.org/10.1016/j.pocean.2016.12.011

Treguier, A. M., de Boyer Montégut, C., Bozec, A., Chassignet, E. P., Fox-Kemper, B., McC. Hogg, A., Iovino, D., Kiss, A. E., Le Sommer, J., Li, Y., Lin, P., Lique, C., Liu, H., Serazin, G., Sidorenko, D., Wang, Q., Xu, X., & Yeager, S. (2023). The mixed-layer depth in the ocean model intercomparison project (omip): Impact of resolving mesoscale eddies. *Geoscientific Model Development*, *16*(13), 3849–3872. https://doi.org/10.5194/gmd-16-3849-2023

Tsujino, H., Urakawa, L. S., Griffies, S. M., Danabasoglu, G., Adcroft, A. J., Amaral, A. E., Arsouze, T., Bentsen, M., Bernardello, R., Böning, C. W., Bozec, A., Chassignet, E. P., Danilov, S., Dussin, R., Exarchou, E., Fogli, P. G., Fox-Kemper, B., Guo, C., Ilicak, M., … Yu, Z. (2020). Evaluation of global ocean–sea-ice model simulations based on the experimental protocols of the ocean model intercomparison project phase 2 (omip-2). *Geoscientific Model Development*, *13*(8), 3643–3708. https://doi.org/10.5194/gmd-13-3643-2020

Tsujino, H., Urakawa, S., Nakano, H., Small, R. J., Kim, W. M., Yeager, S. G., Danabasoglu, G., Suzuki, T., Bamber, J. L., Bentsen, M., Böning, C. W., Bozec, A., Chassignet, E. P., Curchitser, E., Boeira Dias, F., Durack, P. J., Griffies, S. M., Harada, Y., Ilicak, M., … Yamazaki, D. (2018). Jra-55 based surface dataset for driving ocean–sea-ice models (jra55-do). *Ocean Modelling*, *130*, 79–139. https://doi.org/10.1016/j.ocemod.2018.07.002

Turner, J. T. (2015). Zooplankton fecal pellets, marine snow, phytodetritus and the ocean's biological pump. *Progress in Oceanography*, *130*, 205–248. https://doi.org/10.1016/j.pocean.2014.08.005

van Bleijswijk, J. D. L., Kempers, R. S., Veldhuis, M. J., & Westbroek, P. (1994). Cell and growth characteristics of types a and b of emiliania huxleyi (prymnesiophyceae) as determined by flow cytometry and chemical analyses. *Journal of Phycology*, *30*(2), 230–241. https://doi.org/10.1111/j.0022-3646.1994.00230.x

Wang, W.-L., Moore, J. K., Martiny, A. C., & Primeau, F. W. (2019). Convergent estimates of marine nitrogen fixation. *Nature*, *566*(7743), 205–211. https://doi.org/10.1038/s41586-019-0911-2

Welch, H. E. (1968). Relationships between assimiliation efficiencies and growth efficiencies for aquatic consumers. *Ecology*, *49*(4), 755–759. Retrieved July 19, 2022, from http://www.jstor.org/stable/1935541

Westberry, T., Behrenfeld, M. J., Siegel, D. A., & Boss, E. (2008). Carbon-based primary productivity modeling with vertically resolved photoacclimation. *Global Biogeochemical Cycles*, *22*(2). https://doi.org/10.1029/2007GB003078

Woodson, C. B., & Litvin, S. Y. (2015). Ocean fronts drive marine fishery production and biogeochemical cycling. *Proceedings of the National Academy of Sciences*, *112*(6), 1710–1715. https://doi.org/10.1073/pnas.1417143112

Worm, B., Barbier, E. B., Beaumont, N., Duffy, J. E., Folke, C., Halpern, B. S., Jackson, J. B. C., Lotze, H. K., Micheli, F., Palumbi, S. R., Sala, E., Selkoe, K. A., Stachowicz, J. J., & Watson, R. (2006). Impacts of biodiversity loss on ocean ecosystem services. *Science*, *314*(5800), 787–790. https://doi.org/10.1126/science.1132294

Yeager, S. G., Rosenbloom, N., Glanville, A. A., Wu, X., Simpson, I., Li, H., Molina, M. J., Krumhardt, K., Mogen, S., Lindsay, K., Lombardozzi, D., Wieder, W., Kim, W. M., Richter, J. H., Long, M., Danabasoglu, G., Bailey, D., Holland, M., Lovenduski, N., ... King, T. (2022). The seasonal-to-multiyear large ensemble (smyle) prediction system using the community earth system model version 2. *Geoscientific Model Development*, *15*(16), 6451–6493. https://doi.org/10.5194/gmd-15-6451-2022

Yeager, S. G., Chang, P., Danabasoglu, G., Rosenbloom, N., Zhang, Q., Castruccio, F. S., Gopal, A., Cameron Rencurrel, M., & Simpson, I. R. (2023). Reduced Southern Ocean warming enhances global skill and signal-to-noise in an eddy-resolving decadal prediction system. *npj Climate and Atmospheric Science*, *107*(6). https://doi.org/10.1038/s41612-023-00434-y

Ziveri, P., Gray, W. R., Anglada-Ortiz, G., Manno, C., Grelaud, M., Incarbona, A., Rae, J. W. B., Subhas, A. V., Pallacks, S., White, A., Adkins, J. F., & Berelson, W. (2023). Pelagic calcium carbonate production and shallow dissolution in the north pacific ocean. *Nature Communications*, *14*(805). https://doi.org/10.1038/s41467-023-36177-w